

# An ultrafast plenoptic-camera system for high-resolution 3D particle tracking in unsegmented scintillators

Till Dieminger<sup>1</sup>, Saúl Alonso-Monsalve<sup>1</sup>, Christoph Alt<sup>1</sup>, Claudio Bruschini<sup>2</sup>,  
Noemi Bühner<sup>1</sup>, Edoardo Charbon<sup>2</sup>, Kodai Kaneyasu<sup>2</sup>, Tim Weber<sup>1</sup>,  
Matthew Franks<sup>1</sup>, Davide Sgalaberna<sup>1\*</sup>

<sup>1</sup>IPA, ETH Zürich, Otto Stern Weg 5, Zurich, 8093, Zurich, Switzerland.

<sup>2</sup>Advanced Quantum Architecture Lab (AQUA), EPFL, Rue de la Maladière, 2000, Neuchâtel, Switzerland.

\*Corresponding author(s). E-mail(s): [davide.sgalaberna@cern.ch](mailto:davide.sgalaberna@cern.ch);

## Abstract

Neutrino detectors, particle calorimeters and some dark matter detectors require dense and massive active materials. An extremely fine segmentation is desirable to achieve precise three-dimensional particle tracking. However, such systems introduce significant challenges in construction and demand a large number of readout electronics channels, leading to extremely high costs. In this article, we propose an alternative approach to elementary particle detection that enables ultrafast three-dimensional high-resolution imaging in large volumes of unsegmented scintillator. Enabling technologies are plenoptic systems and time-resolving single-photon avalanche diode array imaging sensors. Together, they enabled us, using a plenoptic camera, to reconstruct the origin of single photons in the scintillator. A case study focused on neutrino detection demonstrates full event reconstruction with a spatial resolution of two hundred micrometres. This work paves the way for a class of particle detectors whose capabilities should be further enhanced through future developments and expanded to Cherenkov light detection, medical imaging and neutron detection.

**Keywords:** particle detector, SPAD array sensor, organic scintillator, plenoptic camera, 3D imaging, ray tracing, neutrino detector, deep learning.

## 1 Introduction

Modern elementary particle detectors deployed at high-energy physics experiments often have to cover huge volumes or surfaces and, at the same time, provide a spatial resolution on the order of 100  $\mu\text{m}$  with a time resolution of a few hundred picoseconds or better. Moreover, dense active materials are necessary for detecting weakly interacting particles, such as neutrinos [1–6] and

certain categories of dark matter candidates [7–10], as well as for electromagnetic and hadronic calorimetry [11–15].

Scintillator-based detectors constitute a suitable choice for active, high-density detection systems, offering the potential for sub-millimetre spatial resolution. Organic scintillators emit blue or green isotropic light, typically in the range of 8,000 to 13,000 photons per MeV loss, when traversed by ionising radiation [16], with a decay time down to about 1-2 ns [17, 18]. Advances in

detector technology have enabled 3D segmentation down to 1 cm with sub-nanosecond timing in tonne-scale scintillator volumes with wavelength shifting (WLS) fibre readout [19–23]. R&D on 3D printing of plastic scintillator is also underway [24–30]. Another notable scintillator-based technology, currently under development, aims to get rid of the geometrical segmentation by deploying organic scintillating materials with a short optical scattering length to stochastically contain the visible photons within small localised volumes [31]. These detectors, typically read out by Silicon Photomultipliers (SiPMs) [32], are also suitable for precise time-of-flight measurements of both charged particles [33] and neutrons [34, 35]. In the form of thin scintillating fibres, spatial resolutions below 100  $\mu\text{m}$  can be achieved [36, 37]. However, the main drawback lies in the challenging and costly construction, due to the very large number of channels required, particularly when targeting tonne-scale detectors. However, the main drawback lies in the challenging and costly construction due to the very large number of analog readout channels required, each needing to be instrumented with corresponding digitisation electronics, particularly when targeting tonne-scale detectors.

In recent years, a new class of photosensors has seen tremendous improvements: Single-Photon Avalanche Diode (SPAD) arrays. These arrays consist of multiple photosensitive diodes manufactured in CMOS technology, which are independently read out to provide single-photon images with sub-nanosecond time resolution. They are sometimes also referred to as digital SiPMs. Unlike SiPMs, SPAD arrays integrate readout electronics directly on-chip [38]. Consequently, a single data line allows the readout of millions of pixels, rather than requiring an independent analogue channel and digitisation chain for each. They are well-suited for applications including LIDAR [39], non-line-of-sight Imaging [40], Raman spectroscopy [41], and event cameras [42]. SPAD arrays featuring pixel pitches as small as 2.5  $\mu\text{m}$  [43, 44], or equipped with time-to-digital converters (TDCs) providing timestamp resolutions down to 50 ps [39, 45], have been demonstrated in the literature. Recently, fast CMOS SPAD array sensors have been proposed as a

cost-effective light readout system for scintillating fibre-based particle detectors [46].

The next step in scintillator detectors involves 3D imaging of photon-starved particle events in monolithic volumes. Ref. [47] was able to reconstruct the position of gamma rays with a SPAD array sensor. However, the spatial resolution was limited by the use of the circle of confusion method, applicable only to point-like sources. Other independent works, based on Monte Carlo (MC) simulation studies, have proposed more complex optical systems adopting conventional photosensors to enhance the sensitivity to the spatial depth of particle interactions, showing potential resolutions around 1 to 10 cm, depending on the volume size: array of multiple lenses coupled to photomultiplier tubes (PMTs) for a large-scale unsegmented liquid scintillator detector [48]; coded masks [49] or objective lenses [50] coupled to SiPM to detect vacuum ultraviolet (VUV) scintillation light in liquid argon. In Ref. [51], a system of three objective lenses viewing three orthogonal faces of a few-centimetre plastic scintillator volume for fast neutron detection was studied with MC simulations.

The device with the greatest potential for 3D imaging of photon-starved events is the plenoptic camera. It combines a single main objective lens (main lens) with a micro-lens array (MLA) placed in front of an imaging photosensor. Each micro-lens projected onto a subset of sensor pixels acts as a tiny camera with a slightly different perspective. This enables stereoscopic vision and thus depth reconstruction from a single exposure. A plenoptic camera is capable of capturing the “light field”, described by the function  $\mathcal{L}(x, y, z, \phi, \theta)$ , which encodes the light intensity at each spatial point  $(x, y, z)$  propagating in direction  $(\phi, \theta)$  [52]. For this reason, it is often referred to as a light-field camera. Although the concept dates back to 1908 [53], it is only within the past two decades that the computationally intensive image post-processing has become practical [54–56]. Alternative plenoptic configurations have been proposed [57] and commercialised [58]. Recently, a plenoptic camera instrumented with a charge-coupled device (CCD) sensor has been proposed for 3D particle dosimetry [59]; however, it lacks the timing information and single-photon sensitivity required to resolve images of individual

particles. Closely related to the concept of plenoptic cameras, Ref. [60, 61] investigates a design comprising lens arrays placed on the six faces of a 60 cm plastic scintillator cube, read out using SPAD array imagers, studied through MC simulations for gamma-ray detection via Compton-scattered electrons. As noted by the authors, a principal limitation of the approach is that tracks exceeding beyond the field of view of a single lens cannot be accurately reconstructed, thereby restricting the detector’s capability to the tracking of particles below a certain energy threshold. A plenoptic system is mentioned as an alternative option, but was neither conceptualised nor studied. As of now, the application of plenoptic cameras with sub-nanosecond timing to image particle events remains unexplored.

In this article, we propose and demonstrate a paradigm shift in the detection of particles in a large unsegmented scintillating volume, resulting in high-resolution tracking and calorimetry of multi-particle events. The detector consists of a system of multiple plenoptic cameras, each one with an MLA behind the main lens and a SPAD array sensor with time-resolving capabilities. A pixel pitch of the order of 10  $\mu\text{m}$  is desirable to constrain the light field properly. The post-processing of the 2D photon-starved images captured by the plenoptic cameras provides a pure 3D image by ray-tracing each detected photon back to its origin, leveraging the acquired light field information. If an organic scintillator with a decay time of a few nanoseconds is employed, a single-pixel timestamp resolution on the order of a few hundred picoseconds enables the effective suppression of the dominant fraction of dark counts via time-coincidence techniques. More generally, sub-nanosecond time resolution is often required in particle physics experiments to obtain a high-purity signal sample. The attenuation length, in both its scattering and absorption/emission components, shall be much longer than the size of the detector such that the original directions of the detected photons are preserved. This is easily achievable in organic scintillators with attenuation lengths of a few metres for plastics [17] and a few tens of metres for liquids [62, 63]. In this work, we demonstrate a detector concept with a plenoptic camera instrumented with a SPAD array, and complement it with realistic MC

simulation studies. We developed different methods for image post-processing and a data-driven calibration of the optical model. The first prototype of this detector concept, which we named PLATON-prototype (PLenoptic imAge of Tracked photONs), is shown in Fig. 1. Based on the results of the prototype measurement campaign, we provide the recipe of a future PLATON detector, whose development is underway, determining the design parameters of both the plenoptic system and the SPAD array sensor. We studied its design with a MC simulation of both a large cubic metre size detector as well as in a smaller PLATON-10cm module exposed to an accelerator neutrino beam. A deep neural network (NN), based on the transformer architecture developed initially for large-language models [64, 65], was developed to precisely capture both the lateral and depth spatial information with sub-millimetre resolution. This work lays the foundation for an entirely different approach to detecting elementary particles in dense materials, offering exceptionally high spatial and temporal resolution.

## 2 Results

### 2.1 The PLATON prototype

The PLATON-prototype, shown in Fig. 1, adopts SwissSPAD2 [66] as the imaging sensor. It is a gated SPAD array with a 16.39  $\mu\text{m}$  pixel pitch, a peak photon-detection efficiency of 5% at 520 nm (photon-detection probability of 50% at 520 nm and a fill factor of 10.5%, and no on-chip per-pixel micro-lenses) and a median dark count rate of 0.26 counts per second (cps) per  $\mu\text{m}^2$  of active area. A single image frame corresponds to a gate window that can be varied between 10 ns and 100  $\mu\text{s}$ . The SPAD array returns single-bit frames, where an active pixel indicates that its SPAD has been activated, either by a photon or thermal noise. 2D intensity images with greyscale information are obtained from a stack of multiple frames. The plenoptic system was made in collaboration with Raytrix GmbH [58], which designed and mounted the MLA (f/2.4, micro-lens diameter of 125  $\mu\text{m}$ ). During the assembly process, some glue leaked onto the MLA, making small areas on the left and right sides unusable for accurate imaging. This can be seen in the inset of Fig. 1. A faster MLA, such

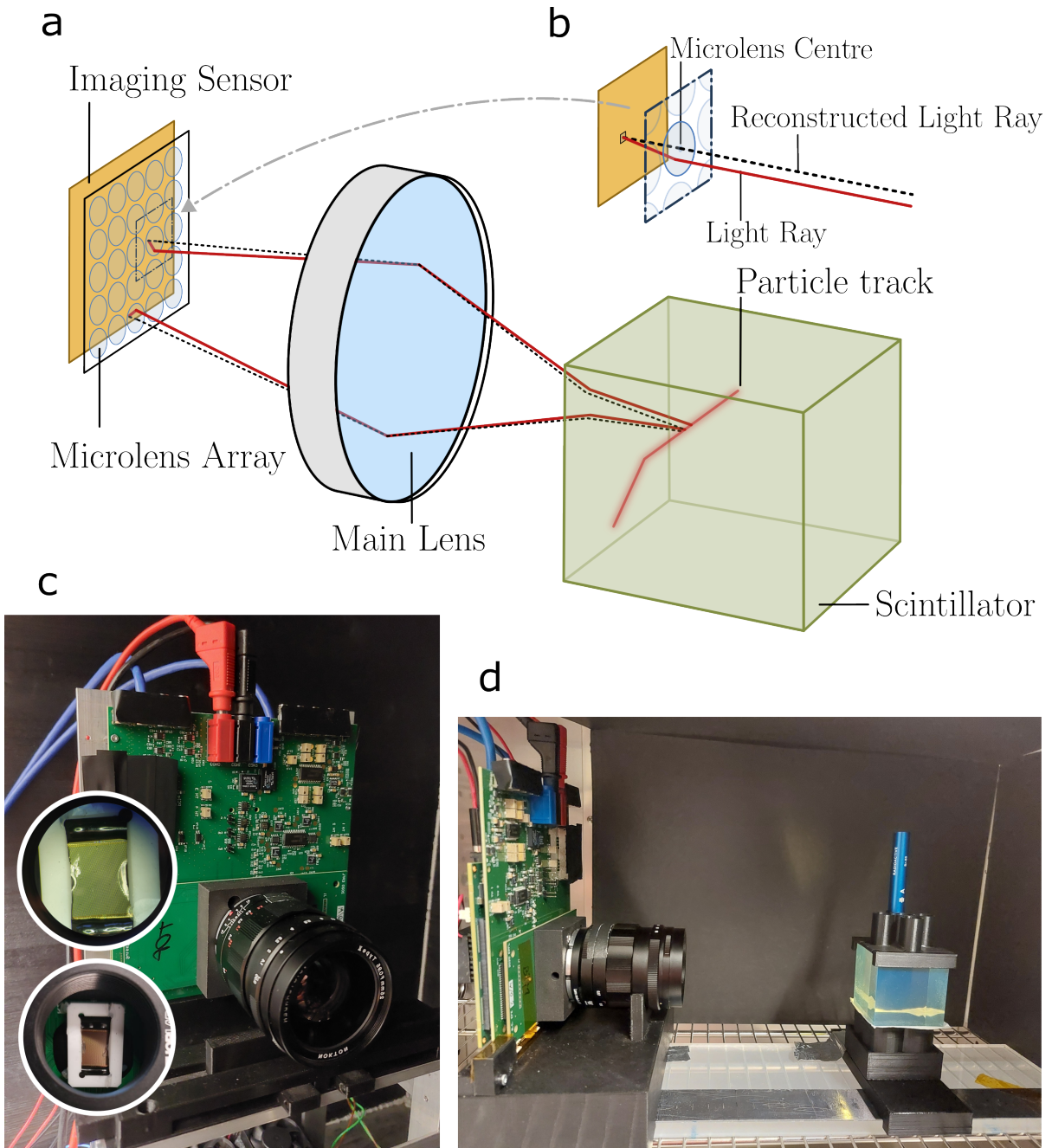


**Fig. 1: PLATON detection and reconstruction principle and the PLATON camera prototype.** **a** The PLATON imaging principle. A plenoptic camera detects photons emitted by a charged particle traversing the scintillator. **b** Principle used to reconstruct single photon micro-images, using the micro-lens centre to determine the angle of the arriving photon. The intersection points of multiple photons are then used to reconstruct the particle track. **c** The PLATON camera prototype. Two insets show the ceramic MLA mount and a microscopy shot of the MLA itself. Here, the spill of the adhesive used to mount the MLA to the ceramic frame on the MLA can be seen on two sides. **d** The experimental setup, measuring  $^{90}\text{Sr}$ -electrons using the PLATON-prototype.

as f/1, desirable to maximise light collection efficiency, could not be used because the glob top, applied to protect the wire bonds of SwissSPAD2, was too thick to place the MLA sufficiently close to the sensor. This limitation will be overcome in a future prototype. A Voigtländer Nokton II 25 mm photographic lens, refitted with a C-Mount, was attached to the printed circuit board, on which the sensor is situated. The focus is set at a 30 cm distance to operate in a focused plenoptic camera mode, with a virtual image being formed behind the sensor. It was operated with f/2.4 to match the f-number of the MLA. With these specifications, we expect a depth resolution of the order of 1 to 5 mm and a sub-mm lateral resolution with a depth of field of 150 mm, calculated based on the effective resolution ratio (ERR) and the overall minimal change in virtual depth, as described in [57]. In the future, a better resolution will be achieved with a higher light collection efficiency and optics, currently constrained by the slower MLA f-number.

## 2.2 3D spatial resolution for a point-like light source

Using a back-illuminated pin-hole ( $\varnothing 50 \mu\text{m}$ ) attached to a motorised movement stage, two samples of data were collected. One was used for calibration, while the other was used for validating the post-processing method. To achieve this, the pinhole was positioned at 168 discrete locations relative to the camera using the motorised stage. These locations are illustrated in Fig. 2. Since the primary objective of this study was to calibrate the camera and evaluate the achievable spatial resolution, these measurements were performed without a scintillator, which would require a simple correction for the refractive index.

The image post-processing was performed as described in Sec. 4.2. The calibration of the PLATON-prototype is discussed in Sec. 4.3. The results of the calibration and the spatial resolution obtained with light intensity images, as well as a function of the number of counts, are shown in Fig. 2. The reconstructed 3D position of the light source was compared to its nominal position on the stage. Justified by its size, significantly smaller than the nominal lateral resolution of the PLATON-prototype, the source was assumed to be point-like. The spatial residual of the depth,

2D and 3D position of the light source is defined as the difference between the true (“t”) and the reconstructed position (“r”):

$$\Delta_{depth} = \sqrt{(z_r - z_t)^2} \quad (1)$$

$$\Delta_{rad} = \sqrt{(x_r - x_t)^2 + (y_r - y_t)^2} \quad (2)$$

$$\Delta_{3D} = \sqrt{(x_r - x_t)^2 + (y_r - y_t)^2 + (z_r - z_t)^2} \quad (3)$$

where  $z$  is the depth along the optical axis of the PLATON-prototype, while  $x$  and  $y$  are the lateral dimensions. The resolution is defined as the 68% 1-sided integral of the residual distribution. The depth, 2D lateral and 3D resolutions in the regime of fully-illuminated frames, i.e. when the light field is captured to the best capability of the camera, are, respectively, 4.2 mm, 1.8 mm and 4.5 mm for the validation sample and 2.2 mm, 0.9 mm and 2.4 mm for the calibration sample. The difference in resolution between the validation and calibration data was found to be affected by remounting the camera on the movement stage between the calibration and validation data runs. This can be seen in the shift in the lateral reconstruction in Fig. 2. Thus, we will refer to the calibration sample to highlight the intrinsic resolution of the PLATON-prototype.

The spatial resolution was also studied as a function of the number of detected photons. A data-driven procedure was adopted: 1,000 photon-starved images were obtained by sampling the pixel position of a certain predetermined number of counts, using the intensity image of the point light source at a specific position as a PDF. With 10 detected photons, the 2D lateral resolution falls below 1.2 mm. As expected, the 3D resolution is dominated by the depth one and becomes worse than 10 mm for fewer than 10 photons. The obtained spatial resolution is consistent with what is expected from the design specifications of the PLATON-prototype, including the reduced FoV (see Sec. 2.1), as well as with results obtained with the optical simulation (see Sec. 4.1). Using the simulated equivalent of the calibration sample, the extracted depth resolution is 2.25 mm, with a 2D radial resolution of 0.5 mm. When accounting for possible systematic uncertainties inherent in the stage and camera setup, these values are

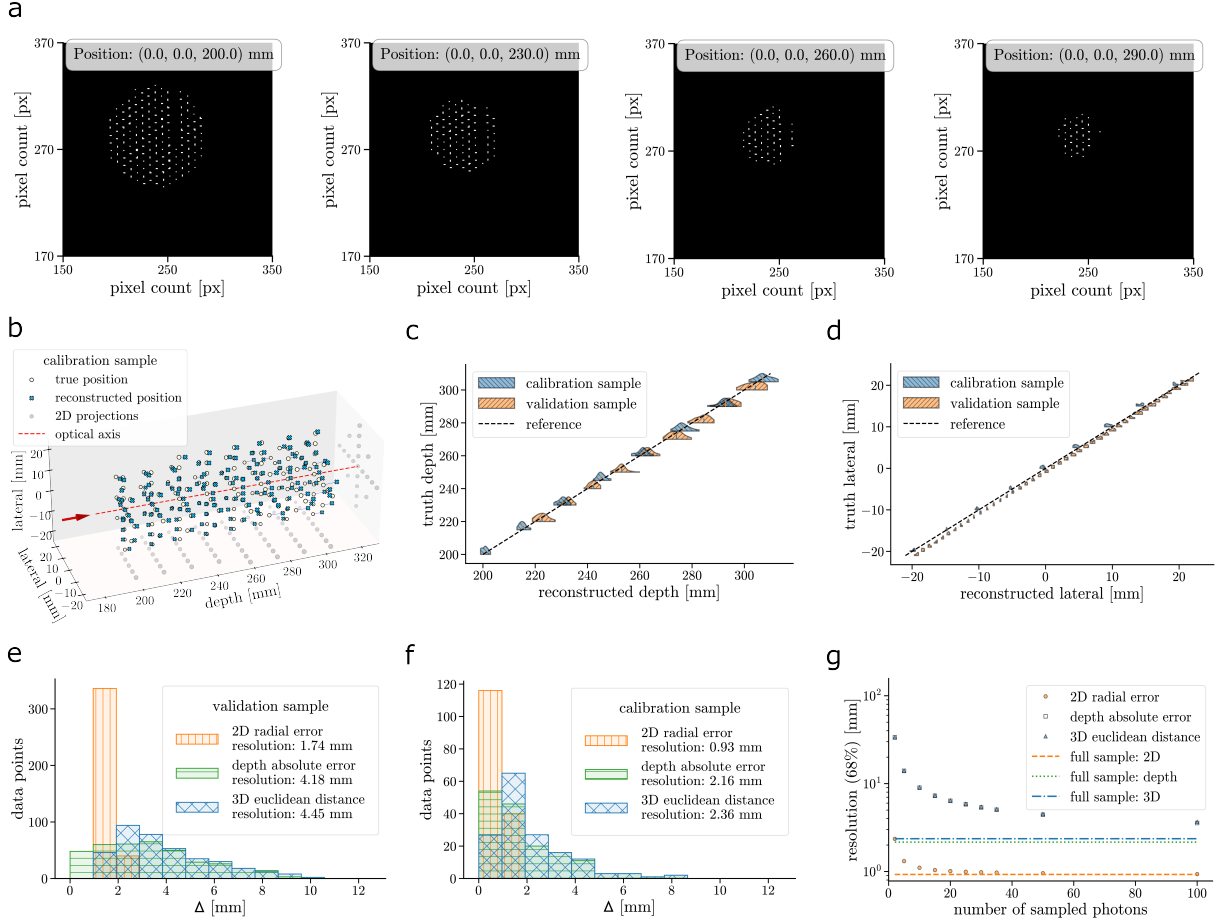


**Fig. 2: Position reconstruction results for a point-like light source with the PLATON-prototype.** **a** Cropped images of the data taken during the calibration measurements. Visible is the calibration point source at different depths, on the optical axis; in classical imaging, the number of micro-images is used to infer the depth of the imaged objects. **b** True (white circles) and reconstructed (blue crosses) positions of the back-lit point light source with respect to the PLATON-prototype. Grey circles indicate the steps done by the moving stage projected onto the two perpendicular planes. The “violin” plots of the reconstructed depth (**c**) and lateral position (**d**) of the light source are shown. The dashed line corresponds to the case of a perfect reconstruction. The probability density function of the source depth or lateral position is shown for the calibration (blue) and validation (yellow) samples. The one-sided distributions of the residuals of the measured 3D positions obtained from the validation (**e**) and calibration (**f**) samples are shown. **g** The depth (green), 2D radial (orange), and 3D (blue) spatial resolutions as a function of the number of photons sampled from the calibration sample are shown on bottom right. The dashed horizontal lines correspond to the resolutions for high yield obtained from **f**.

considered consistent with those obtained from measurements.

An alternative reconstruction method for point-like sources was also tested using a similarly acquired data sample. This method is based on evaluating the likelihood of the measured light

patterns with respect to a reference data sample. A depth resolution of 1.5 mm was achieved along with a lateral resolution of 0.1 mm. With the sampled photon-starved images, the depth and lateral resolutions decreased to, respectively, below 10 mm and 0.3 mm for 5 photons. For fewer than 10 photons, depth ambiguities arise between

points located along a line extending from the principal point, as these produce nearly concentric image patterns. For further details, see Sec. 4.4. It is worth noting that the likelihood study should not be interpreted as the achieved spatial resolution, as it would be impractical to build a PDF for every single possible point down to the relevant precision in a relatively large volume. On the other hand, the largely improved resolution compared to the reference method described in Sec. 2.2 (better than a factor of 2 or 3 for more than 30 counts) indicates that the 2D frames provided by the PLATON-prototype contain more spatial information than what can be exploited with the developed post-processing method. Such a feature highlights that a more advanced post-processing, such as one that uses prior information of the optical model more detailed than that described in Sec. 4.2 or deep learning (see Sec. 2.3.2 and 4.5) would further improve the 3D spatial resolution. Our near-future plan is to pursue both directions further.

### 2.2.1 Detection of $^{90}\text{Sr}$ electron events

The final measurement with the PLATON-prototype aimed to detect, with a plenoptic camera, single elementary particles in plastic scintillator on an event-by-event basis. A  $50\text{ mm} \times 50\text{ mm} \times 50\text{ mm}$  block of EJ-262 plastic scintillator [67] (parameters are listed in Sec. 4.1) was exposed to a  $^{90}\text{Sr}$  source, placed on the top side. The electrons exiting the container of the source can carry an energy up to a maximum of 1.5 MeV. In order to maximise the photon collection, we had to position the scintillator block about 5 cm from the main lens of the PLATON-prototype, just outside the optimal depth of field (150 mm), and hence out of focus. This is limiting the angular resolution on the photon direction. To certify the reconstruction of the electron position, two different datasets were collected, with and without the  $^{90}\text{Sr}$  on top of the scintillator block. We name the two datasets, respectively, as  $^{90}\text{Sr}$  and background. To decrease the probability of dark counts, the PLATON-prototype was placed in a thermal chamber at a temperature of  $-5^\circ\text{C}$ , reducing the median dark count rate (DCR) to  $0.002\text{ cps}/\mu\text{m}^2$  ( $0.4\text{ cps}/\text{pixel}$ ). The background sample allows us to identify noisy pixels, i.e. with a DCR higher than  $0.5\text{ cps}/\text{pixel}$ ,

which were masked at the post-processing stage, further reducing the SwissSPAD2 photodetection efficiency (PDE) down to 2.5%, however increasing the signal-to-noise ratio. Thus, given the limited light yield of the prototype ( $f/2.4$ , active area reduced by the glue), only frames with at least four counts were selected, as these are more likely to contain at least two scintillation photons, necessary to fit a point in the object space. In the post-processing (see Sec. 4.2), candidate photons were identified if the relative minimum distance was less than 3 mm. Out of 9 frames with four counts found in the  $^{90}\text{Sr}$  sample, only four events were selected upon the convergence of the post-processing. As shown in Fig. 3d, for each event the reconstructed position of  $^{90}\text{Sr}$  was closer than 20 mm to its true position, dominated by the depth resolution, as discussed in Sec. 2.2.

This result is consistent, within statistical uncertainty, with the spatial resolution obtained for a low number of photons when accounting for the distance between the main lens and the scintillator, which is not in focus, as shown in Fig. 2.

The same analysis was done on both the  $^{90}\text{Sr}$  and the background sample with frames containing 3 counts. The rejection rates were, respectively, 61% and 81%. In the latter two cases, the distribution of the distance from the  $^{90}\text{Sr}$  nominal position is evenly distributed across the entire depth range. Event displays of the four  $^{90}\text{Sr}$  candidates can be found in Fig. 7. From a toy Monte Carlo simulation of the background sample we expect 0.17 background events with 4 or more counts to be reconstructed between 0 and 20 mm from the true  $^{90}\text{Sr}$  position.

### 2.3 Simulated particle detection with the PLATON-10cm detector

As a physics study case, we chose the detection of GeV muon neutrinos. In fact, the PLATON concept could be suitable for the near detector of future accelerator long-baseline neutrino oscillation (LBL) experiments, which will search for leptonic charge-parity violation and determine the neutrino mass ordering [1–3]. In these experiments, the precise measurement of the neutrino-nucleus cross section is crucial for the reduction of the key systematic uncertainties, and it relies

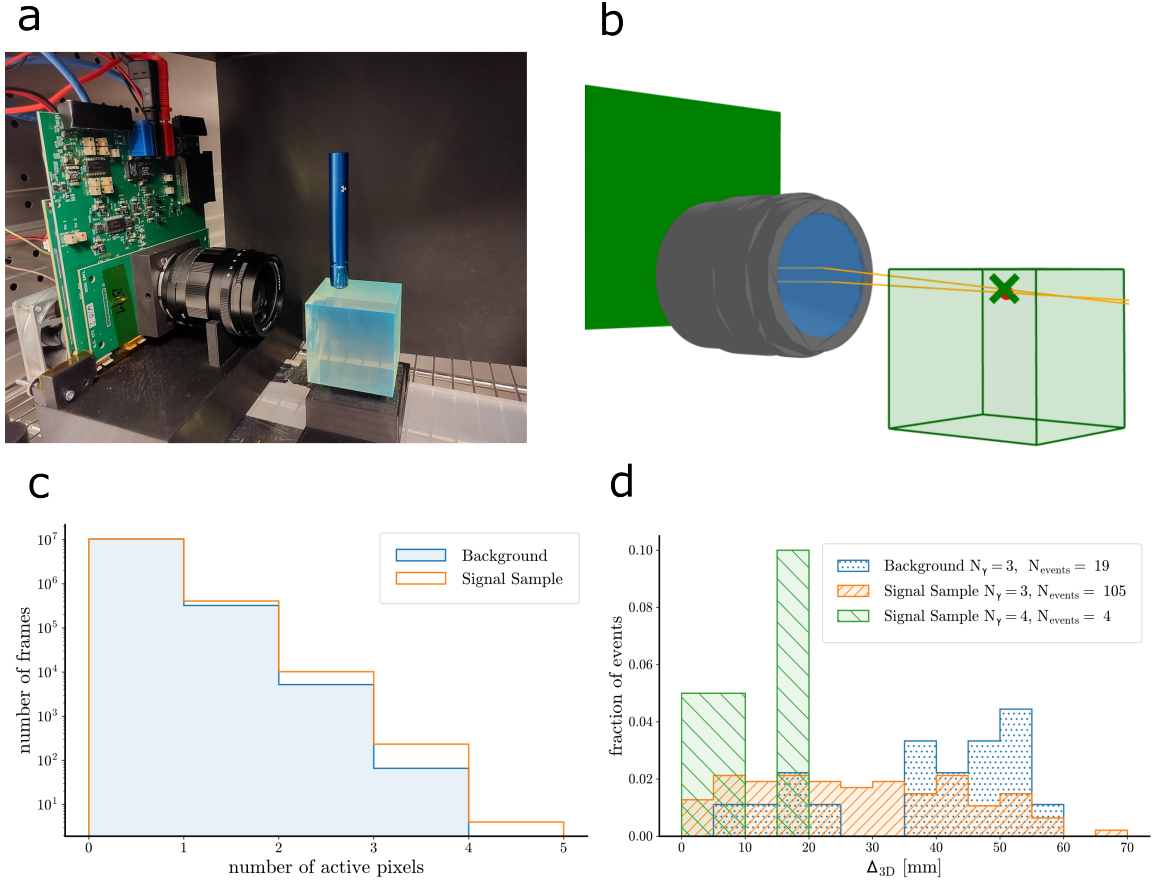


**Fig. 3: Detection of  $\beta$  electrons from a  $^{90}\text{Sr}$  using the PLATON-prototype.** **a** PLATON-prototype pointing to the scintillator block exposed to the  $^{90}\text{Sr}$  positioned on the top face. **b** A candidate electron event in the scintillator (green volume) selected from the  $^{90}\text{Sr}$  sample. The prototype main lens, the reconstructed ray trace of the scintillation photons (orange lines), the nominal position of the source (red dot) and the reconstructed position of the electron (green cross) are shown. Other  $^{90}\text{Sr}$  events can be found in Fig. 7. **c** Distribution of the number of counts per frame for the  $^{90}\text{Sr}$  (orange) and the background (blue) samples. **d** Residual of the reconstructed  $^{90}\text{Sr}$  electron position from the  $^{90}\text{Sr}$  sample with 4 counts (green), 3 counts (orange) and from background sample (blue) with 3 counts.

on the high-resolution tracking and calorimetry of final-state low-momentum hadrons (e.g., multiple protons down to 200 MeV/c). We studied the performance of a small PLATON module consisting of two optical arrays, each of four plenoptic cameras, pointing to two orthogonal faces of a  $10 \times 10 \times 10 \text{ cm}^3$  block of EJ-262 plastic scintillator (parameters are listed in Sec. 4.1), which we call PLATON-10cm. Performing the analysis described below would be challenging for a larger detector volume with the computing power currently available. Since the attenuation length is

way longer than the scintillator volume, a perfect transparency was assumed. This assumption is justified even for larger volumes due to the availability of organic liquid scintillators with analogous light output but attenuation lengths of the order of 20 m or greater [63, 68]. The simulated detector is shown in Fig. 4a. Owing to the results obtained with the PLATON-10cm prototype (see Sec. 2.1), we designed the PLATON-10cm detector unit (a single camera). The adopted strategy consisted of optimising the lateral resolution, with a depth resolution of 1 mm over a depth of field of 10 cm. Exploiting the depth resolution to

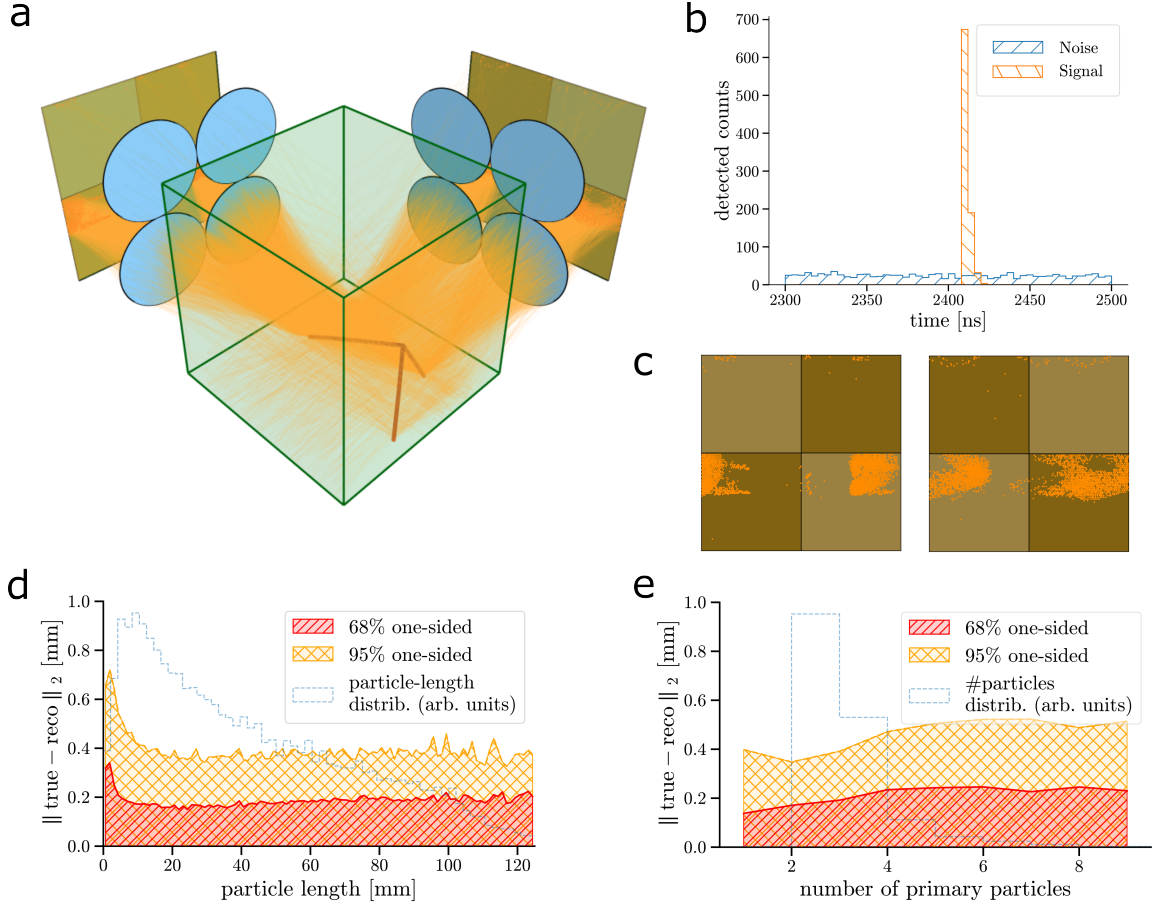


**Fig. 4: Simulation and evaluation results of the proposed PLATON-10cm detector module.** **a** Simulated interaction of a muon neutrino in the PLATON-10cm module. Both the truth particle tracks and the ray traces of the detected photons along with their arrival positions at the SPAD array are shown in different tones of orange. The count time distributions for signal photons (orange) and dark counts (blue) are shown in **b**, while **c** illustrates the frames collected by the SPAD array sensors. 3D spatial resolution as a function of the particle range (**d**) and the number of particles in the event (**e**). Respectively, the distribution of the particle range (**d**) and of the number of particles per event (**e**) is shown (dashed light blue).

match the two orthogonal views, the result is a 3D spatial resolution that mainly belongs to the sub-millimetre lateral one, especially in relatively low-multiplicity events such as neutrino interactions. Both the MLA and the main lens were simulated with  $f/1$ . The diameter of the main lens is 50 mm, while that of the micro-lenses is 1 mm. Realistic parameters of an optimised SPAD array sensor, which we refer to as PLATON SPAD, were simulated. The PDP (40% peak at 500 nm), simulated as in Sec. 4.1 and the pixel pitch of  $25 \mu\text{m}$  with a 60% geometrical fill factor amount to a

PDE of 24%. We neglect the tiling between adjacent photosensors. With all efficiencies accounted for, 3,670 photons were detected per event. The SPAD time structure shown in Fig. 4b was simulated. Each count is measured with a 200 ps resolution timestamp. R&D on PLATON SPAD is ongoing to achieve the parameters above [69].

### 2.3.1 Single-point spatial resolution of an array of multiple cameras

Before studying the capability of a PLATON-10cm module to detect neutrinos, the 3D spatial

resolution for a point light source equivalent to 1 MeV energy deposition was evaluated. Of the 10,000 photons produced, on average 141 photons were detected. The 3D spatial resolution was found to be 0.3 mm. For completeness, we compared plenoptic cameras with classical cameras, obtained by removing the MLA and adapting the lens-sensor distance, focusing the camera on the centre of the scintillator. Here an average of 149 photons were detected per event. While a single classical camera cannot precisely reconstruct the 3D position of the light source, we found that the resolution provided by multiple classical cameras is about four times worse than that of plenoptic cameras. Comparing a setup with two plenoptic cameras to a setup with two classical cameras, we see a significant difference in reconstruction efficiency, indicated in Fig. 8. While the two plenoptic cameras are able in all events to reconstruct the 3D origin of the point source, when the event only falls in the view of a single classical camera, the reconstruction fails, leading to around 23% of failed reconstruction attempts. On the other hand, we note that the size of the scintillator block is not that large and does not require a very long depth of field (DoF), making the performance of an array of classical cameras not too far from that of plenoptic cameras. As we will see later in Sec. 2.4, the resolution of a system of classical cameras deteriorates compared to plenoptic cameras for a  $\text{m}^3$  volume. Thus, we focus on the PLATON-10cm configuration with plenoptic cameras, as described in the previous section. For more details, we refer to Sec. 4.4.1.

### 2.3.2 Neutrino detection in PLATON-10cm

The neutrino flux of the T2K LBL experiment [70, 71] was simulated parallel to both sensor planes, and uniformly in the scintillator volume with the NEUT 5.5.0 event generator [72]. Assuming that an external detector, such as a time projection chamber with a spatial resolution and angular resolution of 1 mm and 0.05 rad respectively in a magnetised volume, would be able to detect and identify the muon escaping the scintillating volume, we simulated a sample of charged-current (CC) neutrino interactions, disregarding the contribution of neutral-current (NC) events.

We developed a custom neural network based on the transformer architecture, commonly used in generative large language models, to efficiently capture the hyper-dimensional correlation between the detected scintillation photons. Details on the neural network are given in Sec. 4.5. We evaluated the particle tracking performance by computing the distance between each point (Geant4 output, see Sec. 4.1) along the truth trajectory of the particle and the closest reconstructed point (Figs. 4d and 4e). Overall, an average 3D-tracking resolution of approximately  $190 \mu\text{m}$  is obtained, with a range of  $150 \mu\text{m}$  to  $340 \mu\text{m}$ . When considering the distance between each reconstructed point and the closest truth point, the resolution becomes more consistent, with a narrower range of  $160 \mu\text{m}$  to  $230 \mu\text{m}$ , though the average remains unchanged. The resolution is smaller than  $200 \mu\text{m}$  for events with three particles or fewer. When particle ranges are less than 3 mm, the resolution averages  $180 \mu\text{m}$ . Overall, the results demonstrate that a tracking accuracy well below 1 mm is achievable within a sizeable PLATON module. This is in agreement with the results of 4.4 and 2.3.1. A pattern recognition algorithm was developed to group the photon origins into different clusters that are then assigned to different particles. The results of the pattern recognition are shown in Fig. 5. The interaction vertex resolution for the full sample of CC interactions is 0.42 mm. The average difference between the number of identified and true particles is 0.25 with a standard deviation of 0.74. More details about the implementation of pattern recognition and particle identification can be found in Sec. 4.6.2.

Two samples of candidate neutrino CC interactions were selected, featuring either a muon and a proton with no pions in the final state (CC  $1\mu 0\pi 1p$ ), or a muon and two protons with no pions (CC  $1\mu 0\pi 2p$ ). The first one is the most common final-state topology below 1 GeV, thus the dominant channel at the T2K and Hyper-Kamiokande LBL experiments, and is mainly affected by CC quasi-elastic (CCQE) interactions, accounting for approximately 37% of all events. The second sample is a golden channel to characterise nuclear processes, such as 2 particle - 2 holes (2p2h) events or final state interactions (FSI) that can introduce biases in the reconstruction of the neutrino energy. The proper theoretical modelling of these

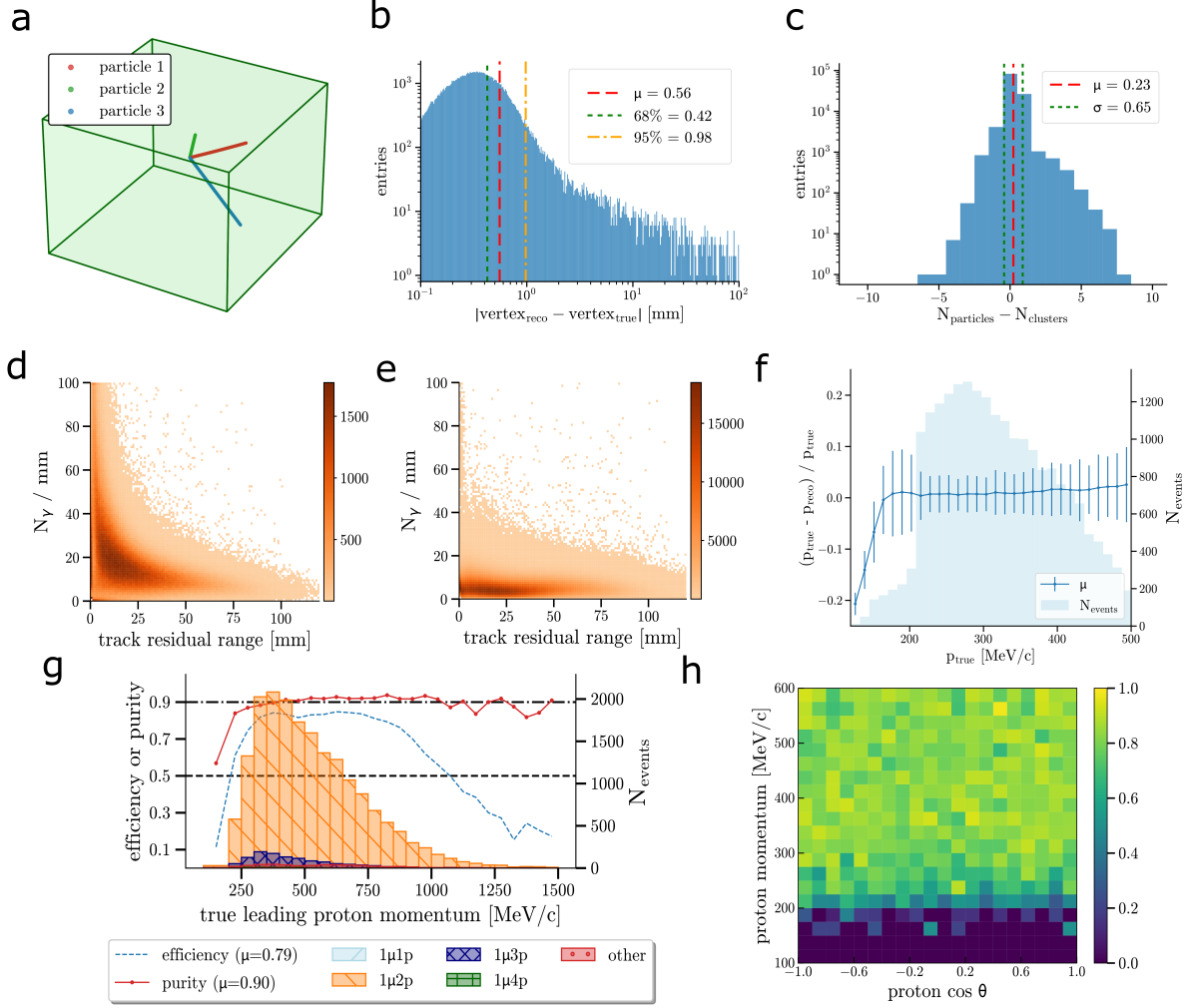


**Fig. 5: Simulated muon neutrino event analysis results.** **a** Particle tracks reconstructed from a CC  $1\mu 0\pi 2p$  neutrino interaction (a muon and two protons with no pions) after applying the image post-processing and the pattern recognition. **b** Residual of the reconstructed neutrino vertex position for proton events. **c** Difference between the number of particles produced by the neutrino interaction and the number of reconstructed clusters for muon events. The measured energy loss by a proton **d** and a muon **e** along the corresponding reconstructed track for all the events. **f** Proton momentum resolution (mean and 68% std) as a function of the stopping proton true momentum for selected CC  $1\mu 0\pi 2p$  events (dark blue line). The true momentum distribution (light blue) of the protons from all the neutrino events is also shown. **g** True momentum distribution of the leading proton in the CC  $1\mu 0\pi 2p$  selected sample, including efficiency and purity. **h** Proton reconstruction efficiency (colour map) as a function of the stopping proton true momentum and angle after applying the CC  $1\mu 0\pi 2p$  selection.

processes is a source of significant uncertainties in LBL experiments. Thus, the precise detection of CC  $1\mu 0\pi 2p$  events is crucial for the precise measurement of neutrino oscillations. More information can be found in Sec. 4.6.3, together with the details of the neutrino event selection.

To demonstrate the capability of a PLATON-10cm detector module to detect neutrinos, we focus on the selection of both CC  $1\mu 0\pi 1p$  and CC  $1\mu 0\pi 2p$  events, noting that the latter are notoriously more challenging to identify due to the presence of higher multiplicity. From Fig. 5f, one

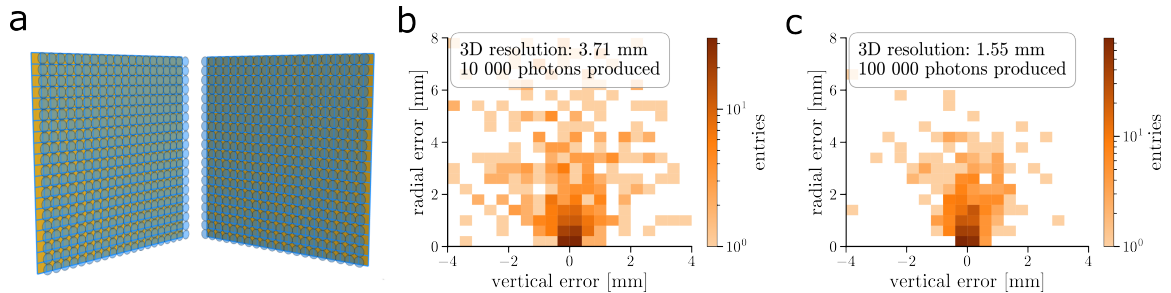


**Fig. 6: Setup and reconstruction of a tonne-scale version using the PLATON detector concept.** **a** The geometry of a tonne-scale  $1 \times 1 \times 1 \text{ m}^3$  PLATON-1m detector. The plenoptic cameras are shown in blue. The same optics configuration as in Sec. 2.3.1 is adopted, resulting in a total of 800 plenoptic cameras, each with about  $4 \times 10^6$  pixels ( $\sim 3.2 \times 10^9$  pixels in total). The spatial resolution in cylindrical coordinates for a point light source emitting **b** 10,000 photons and **c** 100,000 photons is shown.

can see that the momentum of stopping protons reconstructed from the range is inferred with a resolution better than 10% across almost the entire range, approximately 5% at the energy flux peak, and close to 10% only below 200 MeV/c. The CC  $1\mu 0\pi 2p$  selection purity is 90% up to 1.4 GeV/c momentum of the most energetic (leading) proton. The small background contamination comes mostly from events with higher proton multiplicity, typically produced with lower momenta. The total selection efficiency is 78%. It exceeds 80% for leading proton momenta above 300 MeV/c, but drops below 50% for momenta above 1.1 GeV/c, where the muon and the proton become more collinear. The proton reconstruction efficiency, shown for the CC  $1\mu 0\pi 2p$  sample, exhibits a 50% threshold at approximately 215 MeV/c. For the case of CC  $1\mu 0\pi 1p$  events, both the selection efficiency and the purity reach 92%. The direction of single protons is determined with an angular resolution of  $1.5^\circ$ .

The same analysis has also been conducted for a system of classical cameras, as reported in Sec. 4.6.4. When compared to plenoptic cameras, similar conclusions can be drawn, as discussed in Secs. 2.3.1 and 4.4.1.

## 2.4 Single-point spatial resolution at $1 \text{ m}^3$ scale

Finally, the spatial resolution for a point light source in a PLATON detector with a  $1 \times 1 \times 1 \text{ m}^3$  organic scintillator has been studied, named PLATON-1m. Due to limited computational resources, we were unable to perform a

neutrino simulation study similar to the one in Sec. 2.3.2, but we leave it for future work. The same analysis as in Sec. 2.3.1 was performed. As shown in Fig. 6, a 3D spatial resolution of 3.7 mm can be achieved for an energy loss of  $\sim 1$  MeV (10,000 photons generated). For reference, this resolution corresponds to an effective segmentation of approximately 7.5 mm. Unlike a segmented detector, it improves up to 1.5 mm for an energy loss of  $\sim 10$  MeV (100,000 photons generated), with an effective segmentation of 3 mm.

The same analysis was performed with arrays of classical cameras. As anticipated above, this time we found that for a  $1 \text{ m}^3$  size detector, the plenoptic system has a spatial resolution almost 4 times better than that of classical cameras.

With a few improvements, a sub-millimetre spatial resolution in a  $1 \text{ m}^3$  scintillator could be achieved. First, the optical parameters have not been optimised for such a volume but have been kept the same as for the  $10 \times 10 \times 10 \text{ cm}^3$  module. Moreover, the used post-processing method adopts a simplified parametrisation of the MLA. On the other hand, we also observed that the NN described in Sec. 4.5 allowed for an additional improvement in spatial resolution. Thus, one might expect a similar improvement also in the tonne-scale PLATON-1m. It is interesting to note that a smaller pixel pitch, though technically challenging, would allow for better constraint of the light field. Preliminary studies showed 30% improvement in spatial resolution for a  $1 \mu\text{m}$  pitch without any adaptation of the optics.

### 3 Discussion

In this work, we propose a change of paradigm in the high-resolution detection of elementary particles in dense scintillator-based detectors. The key is the use of imaging photosensors with single-photon sub-nanosecond time resolution, such as SPAD array sensors, integrated into a system of plenoptic cameras to provide unambiguous 3D images of elementary particles interacting within a monolithic volume of scintillator. We referred to this detector concept as PLATON.

We built and successfully characterised the spatial resolution of the PLATON detector prototype, a plenoptic camera instrumented with a SPAD array sensor, and we developed a post-processing method suitable for photon-starved images. We also succeeded in reconstructing the position of  $^{90}\text{Sr}$  electrons on an event-by-event basis. All the results are in agreement with our simulations, which gives us confidence in designing a realistic PLATON detector for neutrino detection.

Building on the experience gained through prototyping, we carried out a simulation-based analysis of muon neutrino interactions in a PLATON detector, employing an improved yet realistic design. We developed a high-performance image post-processing based on deep learning and complemented by pattern recognition algorithms. A tracking resolution down to  $200\ \mu\text{m}$ , along with high purities and efficiencies in the selection of neutrino interactions with multi-proton final states, was achieved.

The extrapolation to a 1-tonne scintillator detector showed a spatial resolution of a few millimetres for point light sources. Although it is already competitive with state-of-the-art plastic scintillator detectors, we expect more sophisticated image post-processing, such as deep learning, or a plenoptic system optimised for a metre-scale volume, to be promising solutions for achieving sub-millimetre spatial resolution. Future developments, such as optics optimised for metre-scale volume and smaller pixels will further improve the spatial resolution. This will be the topic of future dedicated work.

We compared the simulation results with those obtained using a system of classical cameras and found that plenoptic cameras outperform classical systems, regardless of the scintillator volume size.

The PLATON detector configuration offers broader applicability beyond accelerator-based neutrino studies, which were adopted here as a case study. Its calorimetric capability combined with high spatial resolution could make this concept potentially suitable for scintillator-based neutrino-less double-beta decay ( $\nu$ -less  $\beta\beta$ ) experiments and makes it worth studying. Examples could be Ref. [73] or large-scale detectors such as Ref. [74–77] (see also Ref. [78] for a comprehensive review). Furthermore, following the design philosophy outlined in Ref. [48], the PLATON concept appears promising for application in very-large-scale neutrino detectors [68, 79–81]. Similarly, it may enhance the reconstruction of light rings characteristic of Cherenkov radiation [82, 83]. Compared to liquid argon time projection chambers (LArTPCs), currently the only technology capable of 3D tracking particles produced by neutrino interactions with O(mm) resolution in giant volumes, the PLATON technology would profit of its much faster response. Thus, it is ideal for the detection and the reconstruction of the time-of-flight of fast neutrons produced by neutrinos. All would be achieved without the need of big cryogenic infrastructures. On the other hand, its scalability to the kilotonne scale achieved by LArTPCs will have to be proven.

To conclude, our work paves the way towards high-resolution particle tracking and calorimetry in unsegmented volumes. The development of SPAD array imaging sensors, or other photosensor technologies with analogous features, is the key. We are currently conducting R&D to develop a SPAD array sensor that meets the requirements discussed in this article, specifically a PDE similar to that of high-dynamic range SiPMs [32] and single-photon sub-nanosecond time resolution.

Owing to high-spatial resolution in large and dense active volumes combined with an excellent time resolution, the PLATON concept therefore naturally opens up new areas of application for deploying plenoptic cameras for imaging, including positron-emission tomography (PET), neutron radiography, muon tomography, synthetic computed tomography (CT), and proton CT.

## 4 Methods

### 4.1 Optical model and simulation

The interaction and propagation of particles in the scintillator volume were simulated with the Geant4 toolkit [84–86]. The parameters of polyvinyltoluene-based plastic scintillator are simulated with light yield (8,700 photons / MeV), emission and absorption spectra, attenuation length (2.5 m), refractive index (1.58), and decay time ( $\sim 2.1$  ns) characteristic of EJ-262 [67], the scintillator used for the PLATON-prototype. It is worth mentioning that the purpose of this simulation study is general and is applicable to a wide variety of organic scintillators, including those in the form of liquid, often used in giant neutrino experiments [68, 79]. Their typical light yield is around 10,000 photons / MeV, attenuation lengths equal or above 20 m, as well as very high purity, thus, a very uniform optical performance.

Neutrinos are simulated as follows. The neutrino energy was simulated according to the flux made public by the T2K experiment, where it is used in the neutrino oscillation data analyses [70, 71]. The flux is peaked at 0.6 GeV and its broad band ranges mainly from 0.2 to 1.5 GeV, with a long tail up to 30 GeV. The T2K neutrino angular distribution is wide, with a standard deviation of about 4 meters at the near detector location [87]. Thus, for simplicity we decided to simulate neutrinos on a fixed direction, parallel to both sensor planes, without loss of generality. The NEUT 5.5.0 neutrino event generator [72], used at the T2K experiment for neutrino data analyses, is used to simulate the neutrino interactions in the scintillator. It provides the list of final-state particles (particle types and corresponding momentum vectors) and the 3D position of the neutrino interaction vertex. Then, the propagation of the final-state particles in matter is simulated using the Geant4 toolkit [84–86]. We assume the distance between the position of the ionising particle and the final emission of the scintillation light to be small compared to the 3D spatial resolution of the PLATON camera [16, 88] and, thus, no additional smearing on the position of the scintillation light emission is applied. The optical photons produced by the scintillation process are propagated using native Geant4 optical photon processes, including absorption and reflections

following the Fresnel equations. The speed of photons in scintillator is about 20 cm / ns. Once the photons leave the scintillator volume, their positions and directions are stored for subsequent processing steps.

The second part of the optical simulation is based on a custom library that simulates lenses, sensors, and refractive surfaces outside the scintillator volume. It performs the ray tracing of each individual photon from the exit point on the scintillator surface to the photosensor, through the plenoptic system. Thin and thick lenses, together with their apertures, are implemented in the paraxial approximation, assuming 100% lens transparency and neglecting optical aberrations. The propagation time of each photon is computed assuming straight-line travel between optical elements and using the speed of light in vacuum. Further, general surfaces can be added to the optical stack by defining their shape using tessellated triangles in an STL file.

The components of the plenoptic camera model include: the MLA, parametrised as an array of thin lenses or as an array of pinholes with constant same pitch; the parameters of the MLA thin-lens model, including the diameter ( $D_\mu$ ) and the lateral position ( $L_\mu$ ) of each micro-lens; and the distance between the MLA and the sensor planes ( $B$ ) and the focal length of the MLA ( $f_{MLA}$ ). The geometry of the MLA accounts for the insensitive areas between adjacent micro-lenses. All the micro-lenses have the same diameter and focal length. The main lens is modelled with the thick-lens equation, which includes its diameter ( $D_L$ ), the position of the two principal planes ( $P_1$  and  $P_2$ ), and the focal length  $f_L$ . This model can be easily converted to that of a thin lens if the two parallel principal planes coincide.

The simulation of the SPAD array sensors was based on the parameters of SwissSPAD2 [66]. The pixel active and dead areas of the SPAD array were simulated as designed, thus with a geometrical fill factor. The photon detection efficiency (PDP) was simulated as a binomial efficiency following the corresponding wavelength spectrum. The DCR was also cross-checked against measurements performed in our laboratory, and where explicitly mentioned, extrapolated to a future, realistic performance. The timestamp of each pixel can be simulated in either self-trigger or gate mode.

The positions and the relative distances of the optical objects were adjusted to reflect the configuration of the PLATON-prototype (see Sec. 4.2 and 4.3) or that of an optimised PLATON detector (see Sec. 2.3). Although this model appears rather simple, it accurately reproduces the actual resolution of the PLATON-prototype.

## 4.2 Image post-processing method

The detection of elementary particles in scintillator requires single-photon detection. Thus, photon-starved images replace the more traditional ones based on light intensity. A post-processing method was developed to backtrace all the photon rays from the image plane (sensor pixels) to the object space (light source).

Post-processing algorithms for plenoptic systems are based on parallax detection and require pattern matching between images observed by different micro-lenses [89]. In this reconstruction regime, a single point source would create a sub-image in a set of neighbouring micro-lenses. If the point source sits in the focus region of the plenoptic camera, each microlens images a single pixel, while a point source out of focus would create a blurred image in each participating microlens. The number of active microlenses is known as Virtual Depth (VD) and is proportional to the physical distance of the object from the main lens, allowing for depth estimation. However, we decided not to adopt this technique as it cannot be easily applied to photon-starved frames, as it would lead to the pattern matching failing. Thus, we require an optical model (see Sec. 4.1) to project each detected photon through the optics into the object space. Post-processing, based on that of a pinhole camera, is also used for plenoptic cameras in light-intensity imaging [90]. In this work, we adopt the same principle to the case of photon-starved images and, thus, developed the following method: the ray trace of every photon that was detected by a pixel of the sensor (a count) is forced to pass through the centre of the closest micro-lens, and interpolated in the object space. The optical model described in Sec. 4.1 was used for the propagation of the ray tracing: the MLA was parametrised as an array of pinholes, and each photon was assumed to have impinged at the centre of the pixel. Outlier ray traces, mainly generated by noise, but also by the

adopted approximation, were iteratively rejected until either a predefined minimum number of rays with the relative closest distance was obtained or the distance between each leftover ray was below a certain threshold. The interpolation with the remaining ray traces was used to estimate the position of the light source.

The constraint on the direction of the photon rays induced by the pinhole approximation makes this method practical, as the computational complexity scales linearly with the number of photons detected. Eventually, the triangulation is performed among the propagated rays in the object space, based on the minimal distance between different rays.

## 4.3 Calibration of the PLATON-prototype

The post-processing of the 2D images relies on the accurate calibration of the optical model of the prototype, that is, the data-driven inference of the model parameters discussed in Sec. 4.1. First, the lateral position of each micro-lens is obtained by illuminating the PLATON-prototype without the main lens with a source of parallel light rays. This was achieved using a low-power laser mounted on a custom-made motorised stage, which could be translated parallel to the MLA plane. A single greyscale intensity image was obtained from 4'096 frames and used to determine the centre of each micro-lens. The mean distance between the centre of two adjacent micro-lenses was computed to derive the parameter  $D_\mu$ . The position of the micro-lenses could not be determined for the entire area of the MLA, as the glue partially covers that region (see Fig. 1). Consequently, that part of the image was not used in the post-processing. This issue reduced the field of view of the PLATON-prototype. Imaging a parallel-light source is not sufficient to infer the remaining parameters of the optical model. Hence, we acquired a dataset consisting of 12-bit images of a back light-illuminated  $50 \mu\text{m}$  pinhole at 168 different positions within an imaging volume of  $4 \times 4 \times 12 \text{ cm}^3$ . Each image was obtained by stacking 4,096 frames, each recorded with a  $10 \mu\text{s}$  gate. The motorised stage, by design, allowed the light source to move in steps of  $10 \mu\text{m}$ . Measurements where the light source fell outside the camera's field of view (FoV), reduced by the glue, were removed from the dataset. In total,

160 images were used to fit the parameters of the optical model using a custom genetic algorithm, in which the post-processing method was iteratively applied and the distance between the reconstructed and true positions was minimised.

The nominal values of  $B$  and  $f_L$  provided by the manufacturers were used as seeds in the fit, while the parameters of the MLA, previously measured with the parallel-light source, were kept fixed.

The optical simulation (see Sec. 4.1) was used to reproduce images from a  $100\ \mu\text{m}$  point source at the same 168 positions as those of the acquired dataset. The focal length of the micro-lens array,  $f_{\text{MLA}}$ , was fixed to its nominal value in the datasheet of the MLA. Then, the simulated images were compared to the corresponding data samples, and good agreement was observed, indicating that the model provides a reasonable representation of the camera’s optical stack.

In addition to the calibration sample, an independent dataset—referred to as the “validation” set—was acquired and used to evaluate the performance of the post-processing method. In this case, 387 different positions were taken with a depth spacing of 10 mm over a range of 80 mm. The lateral spacing was 1 mm, ranging from  $-21$  mm to 21 mm, along one of the lateral axes. The results of the calibration, as well as the obtained spatial resolution on light intensity images as a function of the number of detected photons, are shown in Fig. 2. The validation sample exhibits a spatial resolution slightly inferior to that of the calibration sample. We realised that this was due to a misalignment caused by the disassembly of the experimental setup between the acquisition of the two data samples.

#### 4.4 Data-driven likelihood reconstruction analysis

Alternative post-processing methods were also tested. The first one consists of a data-driven likelihood analysis. The intensity greyscale images for each of the 160 points scanned during the calibration campaign were used as probability density functions (PDFs). To each PDF, the distribution of the dark counts across the pixels, obtained with an independent measurement, is subtracted. This way we could estimate the intrinsic spatial resolution of the plenoptic system for

the case of a negligible contamination from dark counts. This study aims to emulate the scenario of a future SPAD array chip capable of rejecting dark counts by time coincidence by constructing sampled data frames: after subtracting the independently measured dark-count map, we generate low-photon-count binary frames by sampling from the resulting intensity PDFs. See more details in the discussion in Sec. 3. “Sampled” data frames were obtained by randomly throwing the position of the counts from the PDF of a given position of the light source.

In a given sampled frame, each pixel  $i$  can take the value  $n_i = 0$  or 1, following the Bernoulli probability distribution. On the other hand, the probability  $p_i(\vec{y})$  for a pixel to take the value of 1 depends also on the position of the point light source  $\vec{y}$  and is described by the corresponding measured PDF. The corresponding negative log-likelihood is given by the binary cross-entropy ( $BCE$ ), which compares a sampled data frame taken at the position  $\vec{x}$  to the PDF at a position  $\vec{y}$  and is given by

$$BCE(I_{\vec{x}}|\vec{y}) = -\frac{1}{N_{\text{pixels}}} \sum_i^{N_{\text{pixels}}} n_i \log(p_i(\vec{y})) + (1 - n_i) \log(1 - p_i(\vec{y})) \quad (4)$$

where the first term contributes only when the given pixel in the sampled frame takes the value of 1, while the second term contributes when the pixel is 0 and weighs the probability of the pixel to be off. This likelihood definition allows for taking into account both activated and non-activated pixels. The prefactor  $1/N_{\text{pixels}}$  normalises the  $BCE$  to an average contribution per pixel, keeping its scale independent of the number of pixels entering the comparison and without affecting the position of the minimum with respect to  $\vec{y}$ . For each one, the  $BCE$  was computed with respect to the PDF at every scanned position  $\vec{y}$ , and the position yielding the lowest  $BCE$  value was selected as the best-fit estimate. We refer to this approach as the “likelihood” method.

Since the testable resolution of the likelihood method depends on the distance between two adjacent scanned positions, the calibration sample was augmented within a smaller portion of the volume, which was sampled with a higher density of points. At the depths of 245 mm and 345 mm from

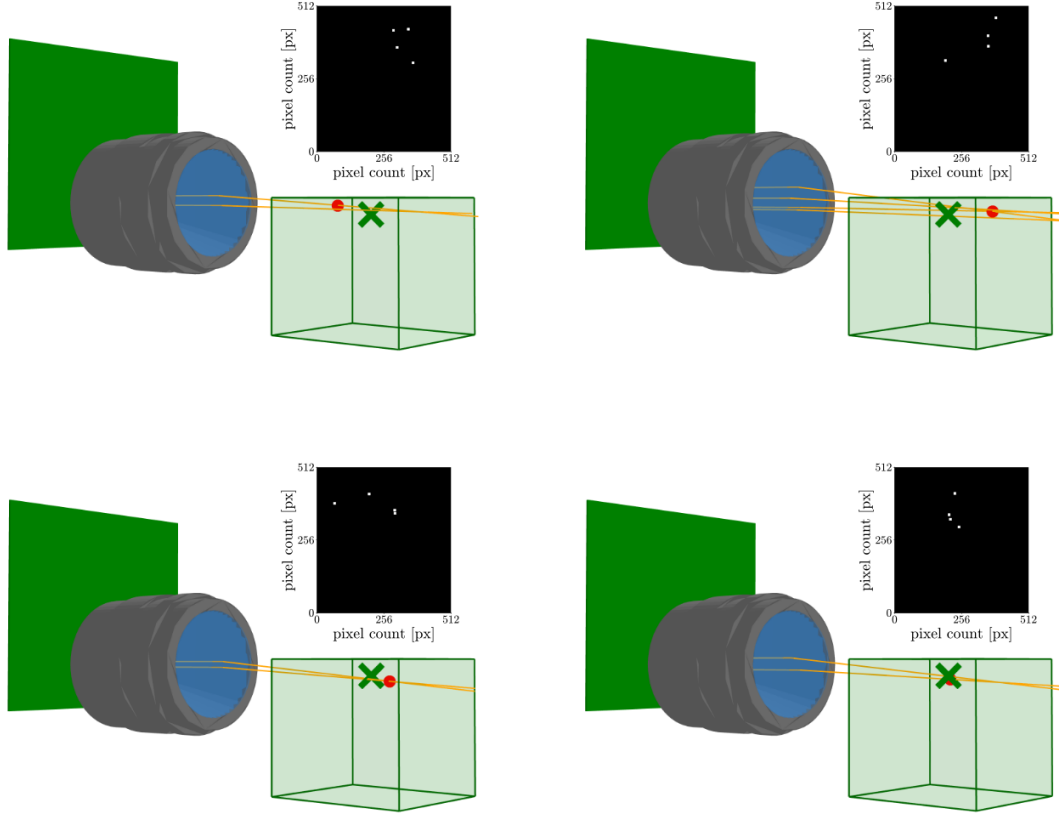


**Fig. 7: Four event displays of reconstructed  $^{90}\text{Sr}$  electron candidates.** Shown are the four identified events, with 4 non masked initial counts on the sensor. For each event the image on the sensor is shown, with enlarged active pixels for visibility. Below each event is shown in an event display, where in orange, the reconstructed rays are visible, together with the real source location (green cross) and the reconstructed point of the  $^{90}\text{Sr}$  (red circle). The data analysis is described in Sec. 2.2.1.

the sensor, 101 16-bit images were taken respectively, with a spacing of 0.1 mm. These were used to determine the lateral resolution. For the depth resolution, data points with a spacing of 1 mm along the optical axis, between a 230 mm and 450 mm distance from the sensor, were gathered. Each of these intensity images was used as an empirical PDF to infer the position of the point light source, and the corresponding sampled low-photon-count datasets were generated as described above.

A depth resolution of 2.5 mm was achieved along with a lateral resolution of 0.1 mm. With the sampled photon-starved images, the depth and lateral residual decreased to, respectively, below 10 mm and 0.3 mm for five photons. Simulation studies have shown that the existence of degeneracies results in an oscillatory pattern in spatial

resolution along both the lateral and depth directions when fewer than 30 counts are detected. This effect is due to statistical fluctuations and is not always reproducible in data, as too many steps of the movement stage and measurements would be needed. Below 10 counts, degeneracies arise also from the fact that points along a single line starting from the principal point of the main lens correspond to concentric images.

#### 4.4.1 Point-light spatial resolution and comparison with classical cameras

Before explicitly studying the capability of a PLATON-10cm module to detect GeV neutrinos, a simulation study was performed to evaluate the

spatial resolution to a point light source corresponding to 1 MeV energy deposition. The post-processing method used to evaluate the spatial resolution for a point light source is the same as described in Sec. 4.2. For a single-point scintillation light source, creating 10,000 photons, the 3D spatial resolution is 0.3 mm. If the number of cameras is reduced to two, the 3D spatial resolution becomes 0.8 mm.

For consistency, we compared the performance of the plenoptic cameras with classical cameras, obtained by removing the MLA and adapting the lens-to-sensor distance. The post-processing adopted for the classical cameras is the same as that used for plenoptic cameras, with the difference that now the pinhole is the main lens. While a single classical camera cannot precisely reconstruct the 3D position of the light source, the resolution of two orthogonal cameras is 2.4 mm, which is three times worse than that of the corresponding plenoptic system. Moreover, we note that two classical cameras fail to reconstruct the position of the light source for approximately 23% of the events, whereas all events are successfully reconstructed for two plenoptic cameras. The resolution for eight cameras, split into two orthogonal views, is approximately four times worse than that of the PLATON-10cm detector module, which utilises eight plenoptic cameras.

Moreover, in the eight-camera setup, 10% of the events with the worst resolution show an average residual of 3.3 mm, which is 4.2 times larger than the case of plenoptic cameras (0.8 mm). This means that plenoptic cameras exhibit a lower probability of making relatively large mistakes in estimating the light source position. The results of the simulation are shown in Fig. 8.

Although an array of classical cameras is capable of reconstructing 3D point-like particle interactions in scintillator, the best performance is provided by an array of plenoptic cameras. Thus, we opted for this latter configuration as baseline for the PLATON detector module in this work.

## 4.5 Neural-network based reconstruction

The dataset used for the neural network studies comprised 1M CC-inclusive muon neutrino interactions generated as described in Sec. 2.3.2. The simulation of the detector setup is discussed

in Sec. 2.3. Reconstructing 3D neutrino interactions within this setup is inherently challenging. SPAD arrays are arranged orthogonally on two sides of the scintillator block. Each interaction produces a photon-starved pattern, typically comprising between a few tens and several thousand detections across the SPADs. The task is to infer the spatial origin and topology of the interaction using only these sparse observations.

To achieve this, we opt for a transformer-encoder-based architecture to fully exploit the spatial correlations among detected photons through the transformer’s attention mechanism [91, 92]. Unlike traditional architectures that rely on local connectivity or fixed sequence order, the transformer’s attention mechanism enables dynamic interactions between all elements in the input. This is particularly beneficial for our application, where the input consists of sparse and spatially-distributed photon detections and where meaningful correlations may exist between distant regions of the detector. Compared to convolutional neural networks (CNNs) [93, 94] or graph neural nets (GNNs) [95–97], which are constrained by local or explicitly defined receptive fields, transformers are not limited to such neighbourhoods and can integrate global spatial context more effectively. Recurrent neural networks (RNNs) [98–100] are also ill-suited for this task, as they assume a consistent sequential ordering, which does not naturally apply to unordered 2D photon hits [101]. In contrast, the transformer’s attention mechanism provides the flexibility to learn arbitrary spatial dependencies, which is essential for resolving the complex and often ambiguous photon distributions resulting from neutrino interactions [102, 103]. An alternative class of models worth considering is Neural Radiance Fields (NeRFs) [104], which learn continuous volumetric scene representations from dense multi-view RGB data using ray-based modelling. While NeRFs have proven effective for reconstructing 3D geometry from 2D projections, their direct application to our setting is limited. SPAD sensors produce extremely sparse, binary detections, lacking the dense photometric supervision and calibrated viewing geometries that NeRFs rely on. Furthermore, NeRFs are primarily designed for photorealistic view synthesis, whereas our goal is to recover the underlying spatial topology of particle interactions from non-image-based,

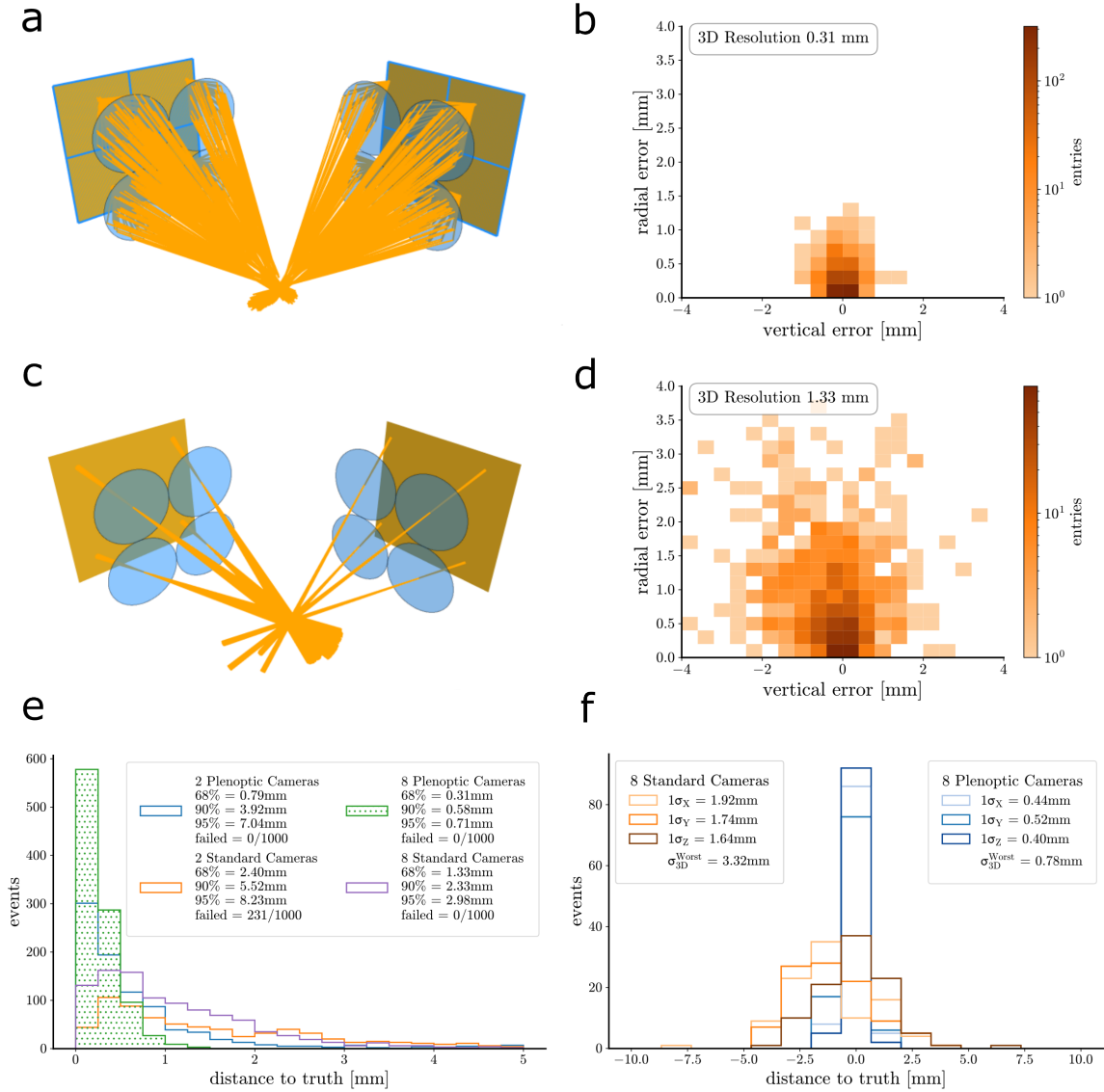


**Fig. 8: Comparison of the performance between plenoptic and standard camera versions of the PLATON detector concept.** Event reconstruction of a simulated point-like light source with eight plenoptic **a** and classical **c** cameras. The spatial residual of the reconstructed vertical position and the cylindrical radial distance from the true origin of photons for eight plenoptic in **b** and standard in **d** cameras. **e** The distributions of 3D spatial residual, i.e., the Euclidean distance between the truth and reconstructed position of the source for 1,000 simulated events for eight and two orthogonal cameras for plenoptic and classical cameras. The legend displays the values of the 68%, 90% and 95% percentiles of the one-sided distribution as well as the number of events for which the post-processing failed. **f** The distribution of the residual of the worst reconstructed 10% of events is shown for both plenoptic (cold-coloured lines) and classical (warm-coloured lines) cameras. The peeling method, described in Sec. 4.2, is not applied to either standard or classical cameras.

unordered data. As such, although NeRF-inspired techniques may hold promise for future work [105, 106], they would require substantial re-engineering to address the unique challenges of our domain. Moreover, more traditional reconstruction methods are discarded due to the multi-dimensional complexity of the problem and the large number of sparse photons involved. These methods often lack the flexibility and computational efficiency required to process and interpret the intricate patterns of photon detection necessary for accurate 3D reconstruction.

We employ a transformer encoder to tackle this reconstruction problem (see Figure 9a). In our setup, each photon is treated as a token, embedding its 2D position on the SPAD array, the identifier of the micro-lens it passed through, and the corresponding SPAD sensor ID. Additionally, the input sequence includes a dedicated token encoding the number of sampled photons in the event and one token for each muon exiting the scintillator block (typically one), which contains the 3D exit point and direction vector. The maximum sequence length is fixed at 1,024 tokens. During training, we randomly select  $\lfloor 0.9N \rfloor$  of photons per event (with  $N$  being the number of photons in the event, further capped by the maximum sequence length) and fill the remainder of the sequence with a padding token, which is ignored during training. This stochastic subsampling means that, from the model’s perspective, the same physical event is seen with a different subset of photons at each epoch, and thus acting as an input-level regularisation/data-augmentation mechanism, reducing overfitting to specific photon patterns and improving generalisation to unseen events. Given that each token already includes spatial information, explicit positional encodings are unnecessary. Early experiments showed that the network struggled to reconstruct events when the number of detected photons was significantly lower than the maximum sequence length. We hypothesise that this limitation arises from the model’s lack of awareness of the photon count in each event. To address this, we include the aforementioned dedicated token encoding the sequence size, which resolves this issue by enabling the model to condition the number of observed photons.

The quadratic complexity  $O(n^2)$  of the standard transformer’s attention mechanism poses

computational challenges for processing events with a large number of photons. To overcome this, we use a custom-adapted version of BigBird’s sparse attention [107], which combines global, window, and random attention within blocks of tokens to achieve linear complexity  $O(n)$  while effectively modelling long-range dependencies. Global attention allows specific tokens to attend to all others, window attention limits tokens to attend only to their neighbours, and random attention randomly connects tokens. This hybrid approach allows the model to handle long sequences while being computationally efficient. In particular, we based our code on HuggingFace’s implementation [108, 109]. Specifically, the BigBird configuration used in our model includes a block size of 64 tokens, with custom modifications to the attention mechanism. Unlike the original BigBird implementation, our configuration does not utilise window attention; each token attends only to itself and not its neighbours (in the sequence space) or tokens within the same block unless that block is selected through random attention. Additionally, global attention is restricted to the global tokens within the first block and does not extend to all tokens in the block. The random attention spans 4 blocks, a value chosen specifically for this setup. These decisions in the attention mechanism arise from the fact that we are not working with true sequential data; the ordering of photons in the input sequence is arbitrary, and we aim to avoid the model learning spurious correlations or patterns from this ordering. Our transformer encoder architecture comprises 12 attention layers, a hidden size of 384 units, GELU activations [110], and 12 attention heads. Shuffling the photon sequence mitigates the risk of the network learning undesirable block patterns.

The Mean Squared Error (MSE) was our first choice as a loss function. It minimises the squared difference between the predicted and true 3D origins of photons. Formally, it is defined as

$$\mathcal{L}_{\text{MSE}} = \frac{1}{N} \sum_{i=1}^N \|\mathbf{y}_i - \hat{\mathbf{y}}_i\|^2, \quad (5)$$

where  $\mathbf{y}_i$  and  $\hat{\mathbf{y}}_i$  denote the true and predicted 3D coordinates of the  $i$ -th photon origin, and  $N$  is the total number of photons.

Initial experiments, however, revealed convergence difficulties due to inherent ambiguities in

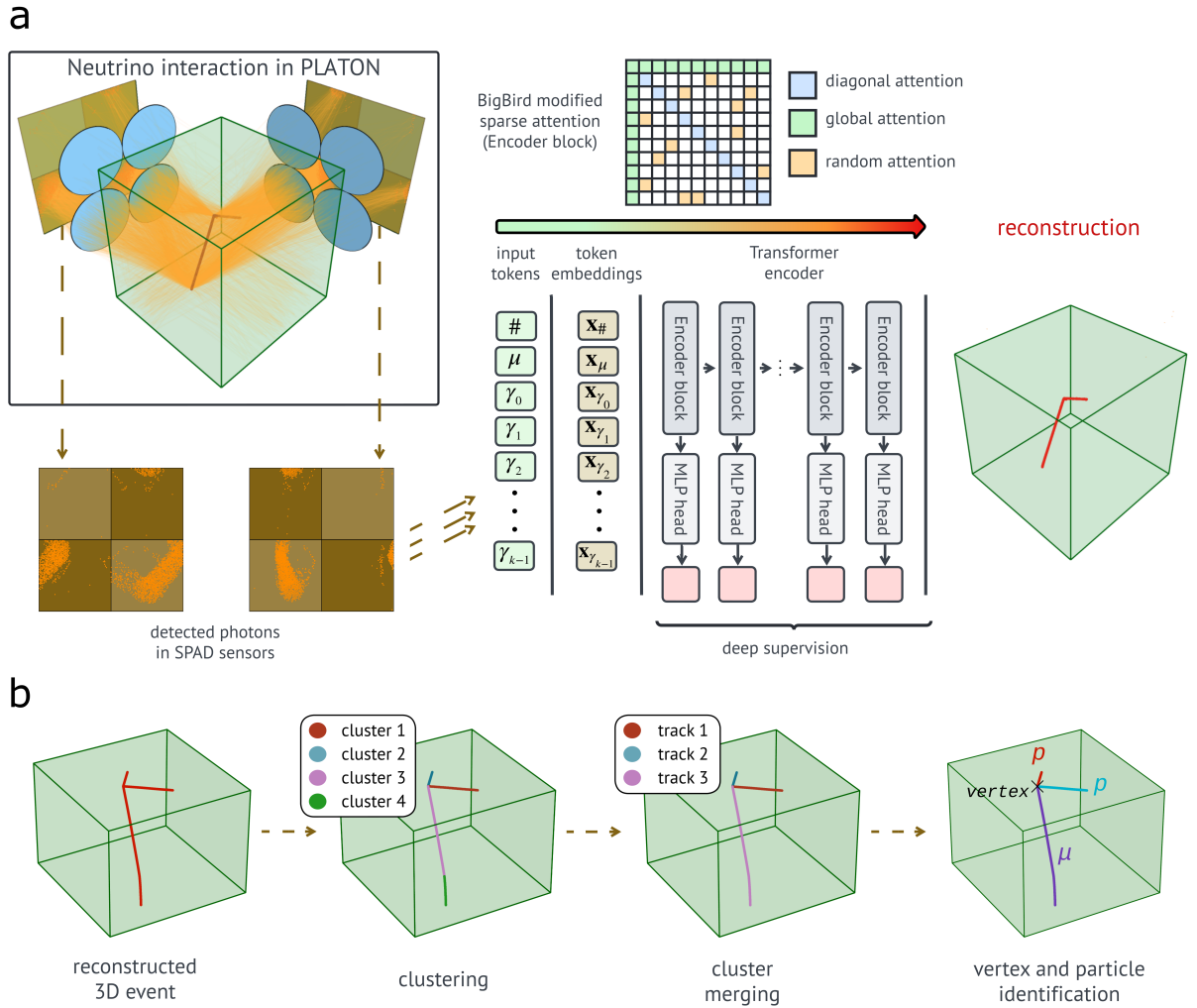


**Fig. 9: Neural event reconstruction and pattern-recognition pipeline.** **a** Neural-network-based reconstruction workflow. From left to right: the detected 2D photon coordinates are grouped into a sequence of tokens  $\gamma$ , with two additional tokens appended:  $\#$ , indicating the total number of photons, and  $\mu$ , optionally encoding the muon’s exiting direction and position. Then, a micro-lens embedding identifying the optical element that detected the photon is summed to the photon coordinate embeddings, and a token type embedding (indicating whether the token represents a photon coordinate, photon count, or muon exiting information) is summed to each token embedding. A modified BigBird Transformer encoder [107] processes the resulting combined embeddings, which leverages diagonal, global, and random sparse attention mechanisms. Finally, multi-layer perceptron (MLP) heads with deep supervision are used to perform the event reconstruction. **b** Pattern recognition steps. From left to right: reconstructed hits are grouped into clusters; collinear and nearby clusters are merged together; finally, particle identification and vertex reconstruction are performed.

photon patterns. To mitigate this, we incorporated the Chamfer Distance (CD), commonly used in the point cloud reconstruction literature. CD relaxes the strict point-to-point correspondence by minimising the distance between each reconstructed point and its closest true point (and vice versa) and is given by:

$$\mathcal{L}_{\text{CD}} = \frac{1}{|\hat{\mathbf{Y}}|} \sum_{\hat{\mathbf{y}} \in \hat{\mathbf{Y}}} \min_{\mathbf{y} \in \mathbf{Y}} \|\hat{\mathbf{y}} - \mathbf{y}\|^2 + \frac{1}{|\mathbf{Y}|} \sum_{\mathbf{y} \in \mathbf{Y}} \min_{\hat{\mathbf{y}} \in \hat{\mathbf{Y}}} \|\mathbf{y} - \hat{\mathbf{y}}\|^2. \quad (6)$$

where  $\mathbf{Y}$  and  $\hat{\mathbf{Y}}$  are the sets of true and predicted 3D points, respectively.

We use CD instead of the Earth Mover’s Distance (EMD) [111] due to EMD’s higher computational complexity and limitations in preserving the fidelity of detailed structures [112]. This approach facilitates learning the overall shape of the neutrino interaction rather than precisely backtracking each individual photon ray. A known limitation of CD is that it does not account for local variations in point density. In regions with low ground-truth density, a single true point may serve as the nearest neighbour for many predicted points, leading to an over-representation of these sparse areas in the loss, while regions with denser ground truth are under-represented. To overcome this limitation, the Density-Aware Chamfer Distance (DCD) [112] is adopted. The DCD augments the CD loss by incorporating a density-aware weighting scheme along with exponential mapping.

For each predicted point  $\hat{y} \in \hat{\mathbf{Y}}$ , denote its nearest neighbour in the true set  $\mathbf{Y}$  and the corresponding squared distance by

$$y^*(\hat{y}) = \arg \min_{y \in \mathbf{Y}} \|\hat{y} - y\|^2, \quad d(\hat{y}) = \|\hat{y} - y^*(\hat{y})\|^2.$$

For each true point  $y \in \mathbf{Y}$ , denote its nearest neighbour in the predicted set  $\hat{\mathbf{Y}}$  and the corresponding squared distance by

$$\hat{y}^*(y) = \arg \min_{\hat{y} \in \hat{\mathbf{Y}}} \|y - \hat{y}\|^2, \quad d(y) = \|y - \hat{y}^*(y)\|^2.$$

In the implementation, the number of times a point is queried is used for density weighting. Let  $n(y^*(\hat{y}))$  be the number of predicted points that select  $y^*(\hat{y})$  as their nearest neighbour, and  $n(\hat{y}^*(y))$  be the number of true points for which

$\hat{y}^*(y)$  is the nearest neighbour. With a small constant  $\varepsilon$  (i.e.,  $1 \times 10^{-12}$ ) and an exponent  $n_\lambda$  (set to 0.5 in our experiments), the weights are given by

$$w(\hat{y}) = \frac{\gamma_{y\hat{y}}}{(n(y^*(\hat{y}))^{n_\lambda} + \varepsilon)}, \quad w(y) = \frac{\gamma_{\hat{y}y}}{(n(\hat{y}^*(y))^{n_\lambda} + \varepsilon)}.$$

Here, the regularisation factors balance the contributions from the two sets and are defined as

$$\gamma_{y\hat{y}} = \frac{n_y}{n_{\hat{y}}}, \quad \gamma_{\hat{y}y} = \frac{n_{\hat{y}}}{n_y}$$

with  $n_{\hat{y}} = |\hat{\mathbf{Y}}|$  and  $n_y = |\mathbf{Y}|$ .

An exponential mapping with scaling factor  $\alpha$  (set to 40 in our experiments) is applied to the squared distances, so that

$$e^{-\alpha d(\hat{y})} \quad \text{and} \quad e^{-\alpha d(y)}$$

map each squared distance to the interval  $(0, 1)$ . Consequently, the Density-Aware Chamfer Distance loss is expressed as

$$\mathcal{L}_{\text{DCD}} = \frac{1}{2} \left( \frac{1}{|\hat{\mathbf{Y}}|} \sum_{\hat{y} \in \hat{\mathbf{Y}}} \left( 1 - w(\hat{y}) e^{-\alpha d(\hat{y})} \right) + \frac{1}{|\mathbf{Y}|} \sum_{y \in \mathbf{Y}} \left( 1 - w(y) e^{-\alpha d(y)} \right) \right). \quad (7)$$

For small distances, the contribution is approximately linear; for larger distances, the contribution saturates, thereby reducing the influence of outliers. The total loss applied to the transformer encoder layers comprises both the DCD and a weighted MSE loss, ensuring a balanced learning process. Deep supervision [113, 114] is applied by computing the loss at each encoder layer with exponentially increasing weights. For a transformer with  $l$  encoder layers, the total loss is

$$\mathcal{L}_{\text{total}} = \sum_{i=1}^l \frac{1}{2^{(l-i)}} (\mathcal{L}_{\text{DCD}} + \beta \mathcal{L}_{\text{MSE}}), \quad (8)$$

where  $\beta$  is a scalar weight that balances the MSE loss with the DCD loss (set to 1 in our experiments), and the factor  $\frac{1}{2^{(l-i)}}$  assigns greater weight to losses computed at deeper layers.

This combined loss function enables learning both the overall geometry and the fine-grained spatial photon distribution effectively, leading to improved convergence and reconstruction quality.

The model was implemented in Python 3.12.2 using PyTorch 2.5.1 [115] and PyTorch Lightning 2.4.0 [116], and trained on a single NVIDIA H100 GPU with 94 GB of memory. The training was conducted over 200 epochs with a batch size of 64 and a maximum input sequence length capped at 1024, as previously specified. The optimiser employed was AdamW [117, 118], with a learning rate initialised at  $2 \times 10^{-4}$ ,  $\beta_1 = 0.9$ ,  $\beta_2 = 0.95$ , and a weight decay of  $10^{-4}$ . The learning rate schedule consisted of a single warm-up epoch, followed by cosine annealing over the remaining 199 epochs, decaying smoothly to zero. Hyperparameter optimisation was conducted using the Optuna framework, enabling efficient search space exploration through automated sampling and pruning strategies [119]. No dropout was applied, as empirical evidence indicated a detrimental effect on the regression of precise continuous values. The generalisation capacity typically provided by dropout was instead achieved through the stochastic sampling of photons per event. Given the large number of possible photon combinations, the likelihood of the model encountering the same subset of inputs across epochs is negligible. All results presented in Sec. 2.3.2 were obtained on the held-out test set from a 60%/10%/30% train/validation/test split, respectively.

## 4.6 Details of the neutrino simulation analysis

### 4.6.1 Post-processing

The neutrino event post-processing consists of the following steps: first, a significant fraction of photosensor dark counts are rejected by signal coincidence in a time window of 10 ns; the 2D images collected by the eight cameras and the muon smeared exiting position (mean = 0 mm, std = 1 mm) and direction (mean = 0 radians, std = 0.05 radians) are given as input to the neural network (NN). No timing information is passed to the NN, which instead returns the 3D origin of each photon associated with a count in the scintillator volume. The result is a cloud of points (“photon

origins”) that indicate the origin of the scintillation photons along the trajectory of every charged particle. This is illustrated in Fig. 4.

### 4.6.2 Pattern recognition

The reconstruction of PLATON 3D images differs from what data processing in particle physics experiments typically requires, and is illustrated in Fig. 9b. The clustering algorithm is based on Gaussian Mixture Model (GMM) [120]: a probabilistic model that represents complex data as a combination of simpler sub-distributions, Gaussian in this case, of underlying hidden classes. The optimal number of clusters was selected using the elbow method, a heuristic that identifies the point beyond which increasing the number of clusters yields only marginal improvements in model performance. In a second step, principal component analysis (PCA) was used to merge clusters into tracks, each assigned to a different particle. This process iterated through all pairs of clusters, merging two clusters if they were both collinear and sufficiently close to each other. Once all the particle tracks of the event were obtained, the vertex of the neutrino interaction was reconstructed. Since the muon is assumed to be determined by an external detector, we use its exiting point on the scintillator surface to assign one of the tracks to the muon. Finally, the extreme of the muon track opposite to its exiting point is identified as the neutrino interaction vertex. In some cases, multiple scattering can break the muon track into different consecutive segments. To overcome this issue, the clustering algorithm is rerun with slightly relaxed conditions, potentially adding a new cluster to the muon track, until a connected but non-collinear cluster is found. If the muon does not escape the scintillator volume, the longest reconstructed track is assigned to it, and the end with the largest number of connected clusters is identified as the interaction vertex. If the two track ends exhibit an equal number of connected clusters, the point forming the smaller angle with the connected cluster is selected as the interaction vertex.

### 4.6.3 Selection of neutrino events

The CC  $1\mu 0\pi 1p$  sample is the most common final-state topology below 1 GeV, observed in experiments such as T2K or Hyper-Kamiokande,

since it is dominated by CC quasi-elastic (CCQE) interactions. Another type of final-state topology is named 2 protons - 2 holes (2p2h) and can be induced by three main types of processes: meson exchange current, where the momentum transfer is shared between two nucleons via the exchange of a virtual meson [121]; short-range nucleon-nucleon correlations (SRC) [122], where the neutrino interacts with a nucleon that is part of a correlated nucleon-nucleon pair and both nucleons are knocked out of the nucleus; FSI, with a nucleon that knocks out a second nucleon. 2p2h events are less frequent ( $\sim 8\%$ ) than CCQE interactions ( $\sim 43\%$ ), but are notoriously affected by significant systematic uncertainties in the modelling of the process [123–125]. Thus, the correct modelling of 2p2h interactions is of vital importance for the ongoing precision measurements of neutrino oscillations [126–129] and, in particular, for the next-generation LBL experiments that will search for leptonic charge-parity violation [3, 130, 131].

The accurate identification of the type of each particle produced by the neutrino interaction relies on the precise measurement of the energy loss along its trajectory. For instance, the detection of the Bragg peak of particles stopping in the scintillator ensures unambiguous particle identification (PID). This feature is enhanced by the fact that most of the muons are produced with a momentum peaked around 0.5 GeV/c with a long tail above 1 GeV, while protons are expected dominantly below 1 GeV/c with a peak around 300 MeV/c. The reconstructed distribution of the energy loss along the track of protons (often stopping in the scintillator) and muons is shown in Fig. 5. To identify the particle type associated with each reconstructed track independently, a boosted decision tree (BDT) classifier was employed using the XGBoost algorithm [132]. The kinematic variables used as input features to the BDT include: the variance of the number of photons per mm, the total number of photons in the track, the maximum number of photons per mm, the minimum number of photons per mm, and the mean number of photons per mm.

#### 4.6.4 Selection of neutrino events with a system of classical cameras

The same study has been conducted with a configuration of the PLATON-10cm module where a

conventional optical system is obtained by removing the MLA. It was found that, although a system based on standard cameras exhibits inferior spatial resolution compared to an equivalent system employing plenoptic cameras (see Sec. 4.4.1), even orthogonal arrays of conventional cameras instrumented with SPAD array sensors can achieve very good performance within a PLATON-10cm module over a range of 10 cm. On the other hand, the drop in selection efficiency below 50% occurs at 215 MeV/c (corresponding to a 3.5 mm proton range) with the MLA, and at 230 MeV/c (corresponding to a 5 mm proton range) without the MLA. A similar difference can be found in the neutrino vertex resolution and the proton angular resolution: the vertex resolution drops from 0.4 mm to 0.6 mm, while the angular resolution falls from  $1.5^\circ$  to  $1.8^\circ$ . This is in line with the results shown in Sec. 4.4.1. Without the MLA, the efficiency and the purity are, respectively, 6% and 5% lower compared to the plenoptic configuration. It is worth noting that the PLATON-10cm module is required to cover a depth of field of 10 cm; therefore, it is plausible that eight classical cameras combined can achieve a reasonably good depth resolution.

## References

- [1] Abe, K., et al.: Sensitivity of the Hyper-Kamiokande experiment to neutrino oscillation parameters using acceleration neutrinos (2025) [arXiv:2505.15019](https://arxiv.org/abs/2505.15019) [hep-ex]
- [2] Abe, K., et al.: Hyper-Kamiokande Design Report (2018) [arXiv:1805.04163](https://arxiv.org/abs/1805.04163) [physics.ins-det]
- [3] Abi, B., *et al.*: Long-baseline neutrino oscillation physics potential of the DUNE experiment. *Eur. Phys. J. C* **80**(10), 978 (2020) <https://doi.org/10.1140/epjc/s10052-020-08456-z> [arXiv:2006.16043](https://arxiv.org/abs/2006.16043) [hep-ex]
- [4] Abe, K., *et al.*: Constraint on the matter-antimatter symmetry-violating phase in neutrino oscillations. *Nature* **580**(7803), 339–344 (2020) <https://doi.org/10.1038/s41586-020-2177-0> [arXiv:1910.03887](https://arxiv.org/abs/1910.03887) [hep-ex]. [Erratum: *Nature* 583, E16 (2020)]

- [5] Acero, M.A., Adamson, P., Aliaga, L., Anfimov, N., Antoshkin, A., Arrieta-Diaz, E., Asquith, L., Aurisano, A., Back, A., Baird, M., *et al.*: Measurement of the  $\nu_e$ -nucleus charged-current double-differential cross section at  $\langle E_\nu \rangle = 2.4$  GeV using nova. *Phys. Rev. Lett.* **130**, 051802 (2023) <https://doi.org/10.1103/PhysRevLett.130.051802>
- [6] Michael, D.G., *et al.*: The Magnetized steel and scintillator calorimeters of the MINOS experiment. *Nucl. Instrum. Meth. A* **596**, 190–228 (2008) <https://doi.org/10.1016/j.nima.2008.08.003> [arXiv:0805.3170](https://arxiv.org/abs/0805.3170) [physics.ins-det]
- [7] Zani, A.: The DarkSide-20k experiment. *JINST* **19**(03), 03058 (2024) <https://doi.org/10.1088/1748-0221/19/03/C03058> [arXiv:2402.07566](https://arxiv.org/abs/2402.07566) [physics.ins-det]
- [8] Acerbi, F., *et al.*: DarkSide-20k sensitivity to light dark matter particles. *Commun. Phys.* **7**(1), 422 (2024) <https://doi.org/10.1038/s42005-024-01896-z> [arXiv:2407.05813](https://arxiv.org/abs/2407.05813) [hep-ex]
- [9] Aprile, E., *et al.*: Projected WIMP sensitivity of the XENONnT dark matter experiment. *JCAP* **11**, 031 (2020) <https://doi.org/10.1088/1475-7516/2020/11/031> [arXiv:2007.08796](https://arxiv.org/abs/2007.08796) [physics.ins-det]
- [10] Aalbers, J., *et al.*: A next-generation liquid xenon observatory for dark matter and neutrino physics. *J. Phys. G* **50**(1), 013001 (2023) <https://doi.org/10.1088/1361-6471/ac841a> [arXiv:2203.02309](https://arxiv.org/abs/2203.02309) [physics.ins-det]
- [11] Andreev, V., *et al.*: A high-granularity plastic scintillator tile hadronic calorimeter with APD readout for a linear collider detector. *Nucl. Instrum. Meth. A* **564**, 144–154 (2006) <https://doi.org/10.1016/j.nima.2006.04.044>
- [12] Repond, J., *et al.*: Hadronic Energy Resolution of a Combined High Granularity Scintillator Calorimeter System. *JINST* **13**(12), 12022 (2018) <https://doi.org/10.1088/1748-0221/13/12/P12022> [arXiv:1809.03909](https://arxiv.org/abs/1809.03909) [physics.ins-det]
- [13] Technical Design Report for the Phase-II Upgrade of the ATLAS Tile Calorimeter
- [14] Abdullin, S., *et al.*: Design, performance, and calibration of CMS hadron-barrel calorimeter wedges. *Eur. Phys. J. C* **55**(1), 159–171 (2008) <https://doi.org/10.1140/epjc/s10052-008-0573-y>
- [15] Chatrchyan, S., *et al.*: Performance and Operation of the CMS Electromagnetic Calorimeter. *JINST* **5**, 03010 (2010) <https://doi.org/10.1088/1748-0221/5/03/T03010> [arXiv:0910.3423](https://arxiv.org/abs/0910.3423) [physics.ins-det]
- [16] Kolanoski, H., Wermes, N.: Particle Detectors. Oxford University Press, Oxford, UK (2020)
- [17] Eljen (2025). [https://eljentechnology.com/images/technical\\_library/Eljen-Catalog-2025-01-web.pdf](https://eljentechnology.com/images/technical_library/Eljen-Catalog-2025-01-web.pdf)
- [18] Artikov, A., Budagov, J., Chirikov-Zorin, I., Chokheli, D., Lyablin, M., Bellettini, G., Menzione, A., Tokar, S., Giokaris, N., Manousakis-Katsikakis, A.: Properties of the Ukrainian polystyrene-based plastic scintillator UPS 923A. *Nucl. Instrum. Meth. A* **555**, 125–131 (2005) <https://doi.org/10.1016/j.nima.2005.09.021>
- [19] Blondel, A., Cadoux, F., Fedotov, S., Khabibullin, M., Khotjantsev, A., Korzenev, A., Kostin, A., Kudenko, Y., Longhin, A., Mefodiev, A., Mermoud, P., Mineev, O., Noah, E., Sgalaberna, D., Smirnov, A., Yershov, N.: A fully-active fine-grained detector with three readout views. *Journal of Instrumentation* **13**(02), 02006–02006 (2018) <https://doi.org/10.1088/1748-0221/13/02/p02006>
- [20] Blondel, A., Bogomilov, M., Bordoni, S., Cadoux, F., Douqa, D., Dugas, K., Ekelof, T., Favre, Y., Fedotov, S., Fransson, K., *et al.*: The SuperFGD prototype charged particle beam tests. *JINST* **15**(12), 12003 (2020) <https://doi.org/10.1088/1748-0221/15/12/P12003> [arXiv:2008.08861](https://arxiv.org/abs/2008.08861) [physics.ins-det]

- [21] Mineev, O., Blondel, A., Favre, Y., Fedotov, S., Khotjantsev, A., Korzenev, A., Kudenko, Y., Mefodiev, A., Noah, E., Sgalaberna, D., Suvorov, S.: Beam test results of 3D fine-grained scintillator detector prototype for a T2K ND280 neutrino active target. *Nuclear Instruments and Methods in Physics Research Section A: Accelerators, Spectrometers, Detectors and Associated Equipment* **923**, 134–138 (2019) <https://doi.org/10.1016/j.nima.2019.01.080>
- [22] Alekseev, I., *et al.*: SuperFGD prototype time resolution studies. *JINST* **18**(01), 01012 (2023) <https://doi.org/10.1088/1748-0221/18/01/P01012> [arXiv:2206.10507](https://arxiv.org/abs/2206.10507) [physics.ins-det]
- [23] Boyarintsev, A., Roeck, A.D., Dolan, S., Gendotti, A., Grynyov, B., Kose, U., Kovalchuk, S., Nepokupnaya, T., Rubbia, A., Sgalaberna, D., Sibilieva, T., Zhao, X.Y.: Demonstrating a single-block 3d-segmented plastic-scintillator detector. *Journal of Instrumentation* **16**(12), 12010 (2021) <https://doi.org/10.1088/1748-0221/16/12/P12010>
- [24] Son, J., Kim, D.G., Lee, S., Park, J., Kim, Y., Schaarschmidt, T., Kim, Y.K.: Improved 3d printing plastic scintillator fabrication. *Journal of the Korean Physical Society* **73**(7), 887–892 (2018)
- [25] Kim, D.-g., Lee, S., Park, J., Son, J., Kim, T.H., Kim, Y.H., Pak, K., Kim, Y.K.: Performance of 3d printed plastic scintillators for gamma-ray detection. *Nuclear Engineering and Technology* **52**(12), 2910–2917 (2020) <https://doi.org/10.1016/j.net.2020.05.030>
- [26] Berns, S., Boyarintsev, A., Hugon, S., Kose, U., Sgalaberna, D., De Roeck, A., Lebedynskiy, A., Sibilieva, T., Zhmurin, P.: A novel polystyrene-based scintillator production process involving additive manufacturing. *JINST* **15**(10), 10 (2020) <https://doi.org/10.1088/1748-0221/15/10/P10019> [arXiv:arXiv:2011.09859](https://arxiv.org/abs/2011.09859) [physics.ins-det]
- [27] Berns, S., Boillat, E., Boyarintsev, A., Roeck, A.D., Dolan, S., Gendotti, A., Grynyov, B., Kose, U., Kovalchuk, S., Li, B., Rubbia, A., Sibilieva, T., Sgalaberna, D., Weber, T., Wuthrich, J., Zhao, X.Y., collaboration, T.D.: Additive manufacturing of fine-granularity optically-isolated plastic scintillator elements. *Journal of Instrumentation* **17**(10), 10045 (2022) <https://doi.org/10.1088/1748-0221/17/10/P10045>
- [28] Sibilieva, T., *et al.*: 3D printing of inorganic scintillator-based particle detectors. *JINST* **18**(03), 03007 (2023) <https://doi.org/10.1088/1748-0221/18/03/P03007> [arXiv:2212.13394](https://arxiv.org/abs/2212.13394) [physics.ins-det]
- [29] Kaplon, L., Kulig, D., Beddar, S., Fiutowski, T., Gorska, W., Hajduga, J., Jurgielewicz, P., Kabat, D., Kalecinska, K., Kopeć, M., *et al.*: Investigation of the light output of 3d-printed plastic scintillators for dosimetry applications. *Radiation Measurements* **158**, 106864 (2022) <https://doi.org/10.1016/j.radmeas.2022.106864>
- [30] Weber, T., Boyarintsev, A., Kose, U., Li, B., Sgalaberna, D., Sibilieva, T., Berns, S., Boillat, E., Roeck, A.D., Dieminger, T., Dolan, S., Franks, M., Grynyov, B., Hugon, S., Jaeschke, C., Rubbia, A.: Additive manufacturing of a 3D-segmented plastic scintillator detector for tracking and calorimetry of elementary particles (2024). <https://arxiv.org/abs/2312.04672>
- [31] Cabrera, A., *et al.*: Neutrino Physics with an Opaque Detector. *Commun. Phys.* **4**, 273 (2021) <https://doi.org/10.1038/s42005-021-00763-5> [arXiv:1908.02859](https://arxiv.org/abs/1908.02859) [physics.ins-det]
- [32] Hamamatsu: MPPC (multi-pixel Photon Counter) S13360 Series. (2022). Accessed 9th of June 2023. [https://www.hamamatsu.com/content/dam/hamamatsu-photonics/sites/dam/hamamatsu-photonics/sites/documents/99\\_SALES\\_LIBRARY/ssd/s13360\\_series\\_kapd1052e.pdf](https://www.hamamatsu.com/content/dam/hamamatsu-photonics/sites/dam/hamamatsu-photonics/sites/documents/99_SALES_LIBRARY/ssd/s13360_series_kapd1052e.pdf)
- [33] Korzenev, A., *et al.*: A  $4\pi$  time-of-flight detector for the ND280/T2K upgrade. *JINST* **17**(01), 01016 (2022) <https://doi.org/10.1088/1748-0221/17/01/P01016>

- [doi.org/10.1088/1748-0221/17/01/P01016](https://doi.org/10.1088/1748-0221/17/01/P01016)  
[arXiv:2109.03078](https://arxiv.org/abs/2109.03078) [physics.ins-det]
- [34] Agarwal, A., *et al.*: Total neutron cross-section measurement on CH with a novel 3D-projection scintillator detector. *Phys. Lett. B* **840**, 137843 (2023) <https://doi.org/10.1016/j.physletb.2023.137843>  
[arXiv:2207.02685](https://arxiv.org/abs/2207.02685) [physics.ins-det]
- [35] Gwon, S., *et al.*: Neutron detection and application with a novel 3D-projection scintillator tracker in the future long-baseline neutrino oscillation experiments. *Phys. Rev. D* **107**(3), 032012 (2023) <https://doi.org/10.1103/PhysRevD.107.032012>  
[arXiv:2211.17037](https://arxiv.org/abs/2211.17037) [hep-ex]
- [36] Joram, C., Uwer, U., Leverington, B.D., Kirn, T., Bachmann, S., Ekelhof, R.J., Müller, J.: LHCb Scintillating Fibre Tracker Engineering Design Review Report: Fibres, Mats and Modules. Technical report, CERN (2015)
- [37] Papa, A., *et al.*: The Mu3e scintillating fiber detector R&D. *Nucl. Instrum. Meth. A* **1050**, 168099 (2023) <https://doi.org/10.1016/j.nima.2023.168099>
- [38] Rochas, A., Gosch, M., Serov, A., Besse, P.A., Popovic, R.S., Lasser, T., Rigler, R.: First fully integrated 2-d array of single-photon detectors in standard cmos technology. *IEEE Photonics Technology Letters* **15**, 963–965 (2003) <https://doi.org/10.1109/lpt.2003.813387>
- [39] Zhang, C., Lindner, S., Antolovic, I.M., Pavia, J.M., Wolf, M., Charbon, E.: A 30-frames/s,  $252 \times 144$  SPAD flash lidar with 1728 dual-clock 48.8-ps tdc, and pixel-wise integrated histogramming. *IEEE J. Solid State Circuits* **54**(4), 1137–1151 (2019) <https://doi.org/10.1109/JSSC.2018.2883720>
- [40] Faccio, D., Velten, A., Wetzstein, G.: Non-line-of-sight imaging. *Nature Reviews Physics* **2**(6), 318–327 (2020) <https://doi.org/10.1038/s42254-020-0174-8>
- [41] Bruschini, C., Homulle, H., Antolovic, I.M., Burri, S., Charbon, E.: Single-photon avalanche diode imagers in biophotonics: review and outlook. *Light Sci Appl* **8**, 87 (2019) <https://doi.org/10.1038/s41377-019-0191-5>
- [42] Sundar, V., Dutson, M., Ardelean, A., Bruschini, C., Charbon, E., Gupta, M.: Generalized event cameras. In: 2024 IEEE/CVF Conference on Computer Vision and Pattern Recognition (CVPR), pp. 25007–25017 (2024). <https://doi.org/10.1109/CVPR52733.2024.02362>
- [43] Morimoto, K., Charbon, E.: High fill-factor miniaturized SPAD arrays with a guard-ring-sharing technique. *Opt. Express* **28**(9), 13068–13080 (2020) <https://doi.org/10.1364/OE.389216>
- [44] Shimada, S., Otake, Y., Yoshida, S., Jibiki, Y., Fujii, M., Endo, S., Nakamura, R., Tsugawa, H., Fujisaki, Y., Yokochi, K., *et al.*: A SPAD Depth Sensor Robust Against Ambient Light: The Importance of Pixel Scaling and Demonstration of a  $2.5\mu\text{m}$  Pixel with 21.8% PDE at 940nm. In: 2022 International Electron Devices Meeting (IEDM), pp. 37–313734 (2022). <https://doi.org/10.1109/IEDM45625.2022.10019414>
- [45] Fischer, P., Zimmermann, R.K., Maisano, B.: CMOS SPAD sensor chip for the readout of scintillating fibers. *Nucl. Instrum. Meth. A* **1040**, 167033 (2022) <https://doi.org/10.1016/j.nima.2022.167033>
- [46] Franks, M., Dieminger, T., Kaneyasu, K., Sgalaberna, D., Bruschini, C., Charbon, E., Kose, U., Li, B., Mos, P., Wayne, M., Weber, T., Wu, J.: Demonstration of particle tracking with scintillating fibres read out by a spad array sensor and application as a neutrino active target. *The European Physical Journal C* **84**(2), 202 (2024) <https://doi.org/10.1140/epjc/s10052-024-12509-y>
- [47] Bocchieri, A., Charbon, E., Velten, A.: Scintillation event imaging with a single photon avalanche diode camera. *Communications Engineering* **3**(1), 135 (2024) <https://doi.org/10.1038/s42254-024-0174-8>

[//doi.org/10.1038/s44172-024-00281-6](https://doi.org/10.1038/s44172-024-00281-6)

- [48] Dalmasson, J., Gratta, G., Jamil, A., Kravitz, S., Malek, M., Wells, K., Bentley, J., Steven, S., Su, J.: Distributed Imaging for Liquid Scintillation Detectors. *Phys. Rev. D* **97**(5), 052006 (2018) <https://doi.org/10.1103/PhysRevD.97.052006> [arXiv:arXiv:1711.09851](https://arxiv.org/abs/1711.09851) [physics.ins-det]
- [49] Andreotti, M., Bernardini, P., Bersani, A., Bertolucci, S., Biagi, S., Branca, A., Brizzolari, C., Brunetti, G., Cagnoli, I., Calabrese, R., *et al.*: Coded masks for imaging of neutrino events. *The European Physical Journal C* **81**(11), 1011 (2021) <https://doi.org/10.1140/epjc/s10052-021-09798-y>
- [50] Cicero, V.: Imaging neutrino interactions with liquid argon scintillation light at the DUNE near detector complex. *Nuclear Instruments and Methods in Physics Research Section A: Accelerators, Spectrometers, Detectors and Associated Equipment*, 170801 (2025) <https://doi.org/10.1016/j.nima.2025.170801>
- [51] Pisanti, C., Berardi, A., Console Camprini, P., Giacomini, F., Massimi, C., Mengarelli, A., Musumarra, A., Pellegriti, M.G., Ridolfi, R., Spighi, R., Terranova, N., Villa, M.: Rip-tide: a proton-recoil track imaging detector for fast neutrons. *Journal of Instrumentation* **19**(02), 02074 (2024) <https://doi.org/10.1088/1748-0221/19/02/C02074>
- [52] Levoy, M., Hanrahan, P.: Light field rendering. In: *Proceedings of the 23rd Annual Conference on Computer Graphics and Interactive Techniques. SIGGRAPH '96*, pp. 31–42. Association for Computing Machinery, New York, NY, USA (1996). <https://doi.org/10.1145/237170.237199> . <https://doi.org/10.1145/237170.237199>
- [53] Lippmann, G.: Épreuves réversibles donnant la sensation du relief. *Journal de Physique Théorique et Appliquée* **7**, 821–825 (1908) <https://doi.org/10.1051/jphysap:019080070082100>
- [54] Adelson, E.H., Wang, J.Y.A.: Single lens stereo with a plenoptic camera. *IEEE Transactions on Pattern Analysis and Machine Intelligence* **14**, 99–106 (1992) <https://doi.org/10.1109/34.121783>
- [55] Ng, R., Levoy, M., Brédif, M., Duval, G., Horowitz, M., Hanrahan, P.: Light field photography with a hand-held plenoptic camera. *CTSR* (2005)
- [56] Ng, R.: Digital light field photography. PhD thesis, Department of Computer Science (2006). <https://people.eecs.berkeley.edu/~textildelowren/thesis/renng-thesis.pdf>
- [57] Perwaß, C., Wietzke, L.: Single lens 3D-camera with extended depth-of-field. In: Rogowitz, B.E., Pappas, T.N., Ridder, H. (eds.) *Human Vision and Electronic Imaging XVII*, vol. 8291, p. 829108. SPIE, Burlingame, CA, USA (2012). <https://doi.org/10.1117/12.909882> . International Society for Optics and Photonics. <https://doi.org/10.1117/12.909882>
- [58] Raytrix GmbH: Raytrix. <https://raytrix.de>. Accessed: 2025-08-01
- [59] Goulet, M., Rilling, M., Gingras, L., Beddar, S., Beaulieu, L., Archambault, L.: Novel, full 3d scintillation dosimetry using a static plenoptic camera. *Medical Physics* **41** (2014) <https://doi.org/10.1118/1.4884036>
- [60] Lebrun, F., Terrier, R., Laurent, P., Prêle, D., Bréelle, E., Baronick, J.-P., Buy, C., Noury, A., Olivetto, C., Chipaux, R.: The Gamma Cube: a novel concept of gamma-ray telescope. In: Takahashi, T., Herder, J.-W.A., Bautz, M. (eds.) *Space Telescopes and Instrumentation 2014: Ultraviolet to Gamma Ray*, vol. 9144, p. 91440. SPIE, Montreal, QC, Canada (2014). <https://doi.org/10.1117/12.2055951> . International Society for Optics and Photonics. <https://doi.org/10.1117/12.2055951>
- [61] Lebrun, F., Terrier, R., Prêle, D., Pellion, D., Ginjac, D., Chipaux, R., Bréelle, E., Laurent, P., Baronick, J.-P., Noury, A., Buy, C., Olivetto, C.: The Gamma Cube: a new way to explore the gamma-ray sky. *PoS*

- Integral2014**, 040 (2015) <https://doi.org/10.22323/1.228.0040>
- [62] Djurcic, Z., et al.: JUNO Conceptual Design Report (2015) [arXiv:arXiv:1508.07166](https://arxiv.org/abs/1508.07166) [physics.ins-det]
- [63] A., A., *et al.*: Optimization of the juno liquid scintillator composition using a daya bay antineutrino detector. Nuclear Instruments and Methods in Physics Research Section A: Accelerators, Spectrometers, Detectors and Associated Equipment **988**, 164823 (2021) <https://doi.org/10.1016/j.nima.2020.164823>
- [64] Vaswani, A., Shazeer, N., Parmar, N., Uszkoreit, J., Jones, L., Gomez, A.N., Kaiser, L., Polosukhin, I.: Attention Is All You Need. arXiv (2017). <https://doi.org/10.48550/ARXIV.1706.03762> . <https://arxiv.org/abs/1706.03762>
- [65] Kora, R., Mohammed, A.: A comprehensive review on transformers models for text classification. In: 2023 International Mobile, Intelligent, and Ubiquitous Computing Conference (MIUCC), pp. 1–7 (2023). <https://doi.org/10.1109/MIUCC58832.2023.10278387>
- [66] Ulku, A.C., Bruschini, C., Antolovic, I.M., Kuo, Y., Ankri, R., Weiss, S., Michalet, X., Charbon, E.: A 512 × 512 spad image sensor with integrated gating for widefield flim. IEEE Journal of Selected Topics in Quantum Electronics **25**, 1–12 (2019) <https://doi.org/10.1109/jstqe.2018.2867439>
- [67] Eljen: Green Emitting Plastic Scintillator EJ-260 and EJ-262. (2016). <https://eljentechnology.com/products/plastic-scintillators/ej-260-ej-262>
- [68] Abusleme, A., *et al.*: JUNO physics and detector. Prog. Part. Nucl. Phys. **123**, 103927 (2022) <https://doi.org/10.1016/j.pnpnp.2021.103927> [arXiv:2104.02565](https://arxiv.org/abs/2104.02565) [hep-ex]
- [69] Kaneyasu, K., Dieminger, T., Franks, M., Sgalaberna, D., Bruschini, C., Charbon, E.: PlatonSPAD: A novel SPAD sensor for large-scale high-resolution particle detectors. In: Proceedings of the International Image Sensor Workshop (IISW), pp. 1–4 (2025)
- [70] Abe, K., et al.: Measurements of neutrino oscillation in appearance and disappearance channels by the T2K experiment with  $6.6 \times 10^{20}$  protons on target. Physical Review D **91** (2015) <https://doi.org/10.1103/physrevd.91.072010>
- [71] T2K Beam Group, W.: Neutrino Beam Flux Prediction 2016. The T2K Experiment (2016). <https://t2k-experiment.org/results/neutrino-beam-flux-prediction-2016/>
- [72] Hayato, Y., Pickering, L.: The neut neutrino interaction simulation program library. The European Physical Journal Special Topics **230**, 4469–4481 (2021) <https://doi.org/10.1140/epjs/s11734-021-00287-7>
- [73] Arnold, R., *et al.*: Probing new physics models of neutrinoless double beta decay with supernemo. The European Physical Journal C **70**(4), 927–943 (2010) <https://doi.org/10.1140/epjc/s10052-010-1481-5>
- [74] Abe, S., et al.: Search for Majorana Neutrinos with the Complete KamLAND-Zen Dataset (2024) [arXiv:2406.11438](https://arxiv.org/abs/2406.11438) [hep-ex]
- [75] Albanese, V., *et al.*: The SNO+ experiment. JINST **16**(08), 08059 (2021) <https://doi.org/10.1088/1748-0221/16/08/P08059> [arXiv:2104.11687](https://arxiv.org/abs/2104.11687) [physics.ins-det]
- [76] Auty, D.J., Bartlett, D., Biller, S.D., Chauhan, D., Chen, M., Chkvorets, O., Connolly, S., Dai, X., Fletcher, E., Frankiewicz, K., *et al.*: A method to load tellurium in liquid scintillator for the study of neutrinoless double beta decay. Nuclear Instruments and Methods in Physics Research Section A: Accelerators, Spectrometers, Detectors and Associated Equipment **1051**, 168204 (2023) <https://doi.org/10.1016/j.nima.2023.168204>
- [77] Anderson, M.R., *et al.*: Development,

- characterisation, and deployment of the SNO+ liquid scintillator. *JINST* **16**(05), 05009 (2021) <https://doi.org/10.1088/1748-0221/16/05/P05009> [arXiv:2011.12924](https://arxiv.org/abs/2011.12924) [physics.ins-det]
- [78] Dolinski, M.J., Poon, A.W.P., Rodejohann, W.: Neutrinoless Double-Beta Decay: Status and Prospects. *Ann. Rev. Nucl. Part. Sci.* **69**, 219–251 (2019) <https://doi.org/10.1146/annurev-nucl-101918-023407> [arXiv:arXiv:1902.04097](https://arxiv.org/abs/1902.04097) [nucl-ex]
- [79] An, F.P., *et al.*: Observation of electron-antineutrino disappearance at Daya Bay. *Phys. Rev. Lett.* **108**, 171803 (2012) <https://doi.org/10.1103/PhysRevLett.108.171803> [arXiv:arXiv:1203.1669](https://arxiv.org/abs/1203.1669) [hep-ex]
- [80] Abreu, M., *et al.*: First Evidence of Solar Neutrino Interactions on C13. *Phys. Rev. Lett.* **135**(24), 241803 (2025) <https://doi.org/10.1103/1frl-95gj> [arXiv:2508.20844](https://arxiv.org/abs/2508.20844) [nucl-ex]
- [81] Askins, M., *et al.*: THEIA: an advanced optical neutrino detector. *Eur. Phys. J. C* **80**(5), 416 (2020) <https://doi.org/10.1140/epjc/s10052-020-7977-8> [arXiv:1911.03501](https://arxiv.org/abs/1911.03501) [physics.ins-det]
- [82] Jiang, M., *et al.*: Atmospheric Neutrino Oscillation Analysis with Improved Event Reconstruction in Super-Kamiokande IV. *PTEP* **2019**(5), 053–01 (2019) <https://doi.org/10.1093/ptep/ptz015> [arXiv:arXiv:1901.03230](https://arxiv.org/abs/1901.03230) [hep-ex]
- [83] Perego, D.L.: The ring imaging cherenkov detectors of the lhcb experiment. *Physics Procedia* **37**, 606–612 (2012) <https://doi.org/10.1016/j.phpro.2012.02.414>. Proceedings of the 2nd International Conference on Technology and Instrumentation in Particle Physics (TIPP 2011)
- [84] Allison, J., Amako, K., Apostolakis, J., Araujo, H., Arce Dubois, P., Asai, M., Barrand, G., Capra, R., Chauvie, S., Chytracek, R., *et al.*: Geant4 developments and applications. *IEEE Transactions on Nuclear Science* **53**, 270–278 (2006) <https://doi.org/10.1109/tns.2006.869826>
- [85] Agostinelli, S., Allison, J., Amako, K., Apostolakis, J., Araujo, H., Arce, P., Asai, M., Axen, D., Banerjee, S., Barrand, G., *et al.*: Geant4—a simulation toolkit. *Nuclear Instruments and Methods in Physics Research Section A: Accelerators, Spectrometers, Detectors and Associated Equipment* **506**, 250–303 (2003) [https://doi.org/10.1016/s0168-9002\(03\)01368-8](https://doi.org/10.1016/s0168-9002(03)01368-8)
- [86] Allison, J., Amako, K., Apostolakis, J., Arce, P., Asai, M., Aso, T., Bagli, E., Bagulya, A., Banerjee, S., Barrand, G., *et al.*: Recent developments in geant4. *Nuclear Instruments and Methods in Physics Research Section A: Accelerators, Spectrometers, Detectors and Associated Equipment* **835**, 186–225 (2016) <https://doi.org/10.1016/j.nima.2016.06.125>
- [87] Abe, K., *et al.*: T2K neutrino flux prediction. *Phys. Rev. D* **87**(1), 012001 (2013) <https://doi.org/10.1103/PhysRevD.87.012001> [arXiv:1211.0469](https://arxiv.org/abs/1211.0469) [hep-ex]. [Addendum: *Phys.Rev.D* 87, 019902 (2013)]
- [88] Tanabashi, M., Hagiwara, K., Hikasa, K., Nakamura, K., Sumino, Y., Takahashi, F., Tanaka, J., Agashe, K., Aielli, G., Amsler, C., *et al.*: Review of particle physics. *Phys. Rev. D* **98**, 030001 (2018) <https://doi.org/10.1103/PhysRevD.98.030001>
- [89] Konz, J., Zeller, N., Quint, F., Stilla, U.: Depth estimation from micro images of a plenoptic camera. In: *BW-CAR Symposium on Information and Communication Systems (SInCom)* (2016)
- [90] Hahne, C., Aggoun, A., Velisavljevic, V., Fiebig, S., Pesch, M.: Baseline and triangulation geometry in a standard plenoptic camera. *International Journal of Computer Vision* **126**(1), 21–35 (2018) <https://doi.org/10.1007/s11263-017-1036-4>
- [91] Vaswani, A., Shazeer, N., Parmar, N., Uszkoreit, J., Jones, L., Gomez, A.N., Kaiser, L., Polosukhin, I.: Attention is all

- you need. In: *Advances in Neural Information Processing Systems*, vol. 30. Curran Associates, Inc., Red Hook, NY, USA (2017). [https://proceedings.neurips.cc/paper\\_files/paper/2017/file/3f5ee243547dee91fbd053c1c4a845aa-Paper.pdf](https://proceedings.neurips.cc/paper_files/paper/2017/file/3f5ee243547dee91fbd053c1c4a845aa-Paper.pdf)
- [92] Niu, Z., Zhong, G., Yu, H.: A review on the attention mechanism of deep learning. *Neurocomputing* **452**, 48–62 (2021) <https://doi.org/10.1016/j.neucom.2021.03.091>
- [93] LeCun, Y., Boser, B., Denker, J.S., Henderson, D., Howard, R.E., Hubbard, W., Jackel, L.D.: Backpropagation applied to handwritten zip code recognition. *Neural Computation* **1**(4), 541–551 (1989) <https://doi.org/10.1162/neco.1989.1.4.541>
- [94] Li, Z., Liu, F., Yang, W., Peng, S., Zhou, J.: A survey of convolutional neural networks: Analysis, applications, and prospects. *IEEE Transactions on Neural Networks and Learning Systems* **33**(12), 6999–7019 (2022) <https://doi.org/10.1109/TNNLS.2021.3084827>
- [95] Scarselli, F., Gori, M., Tsoi, A.C., Hagenbuchner, M., Monfardini, G.: The graph neural network model. *IEEE Transactions on Neural Networks* **20**(1), 61–80 (2009) <https://doi.org/10.1109/TNN.2008.2005605>
- [96] Wu, Z., Pan, S., Chen, F., Long, G., Zhang, C., Yu, P.S.: A comprehensive survey on graph neural networks. *IEEE Transactions on Neural Networks and Learning Systems* **32**(1), 4–24 (2021) <https://doi.org/10.1109/TNNLS.2020.2978386>
- [97] Zhou, J., Cui, G., Hu, S., Zhang, Z., Yang, C., Liu, Z., Wang, L., Li, C., Sun, M.: Graph neural networks: A review of methods and applications. *AI Open* **1**, 57–81 (2020) <https://doi.org/10.1016/j.aiopen.2021.01.001>
- [98] Jordan, M.I.: Chapter 25 - serial order: A parallel distributed processing approach. In: Donahoe, J.W., Packard Dorsel, V. (eds.) *Neural-Network Models of Cognition*. *Advances in Psychology*, vol. 121, pp. 471–495. North-Holland, Amsterdam, Netherlands (1997). [https://doi.org/10.1016/S0166-4115\(97\)80111-2](https://doi.org/10.1016/S0166-4115(97)80111-2). <https://www.sciencedirect.com/science/article/pii/S0166411597801112>
- [99] Jain, L.C., Medsker, L.R.: *Recurrent Neural Networks: Design and Applications*, 1st edn. CRC Press, Inc., USA (1999)
- [100] Sherstinsky, A.: Fundamentals of recurrent neural network (RNN) and long short-term memory (LSTM) network. *Physica D: Non-linear Phenomena* **404**, 132306 (2020) <https://doi.org/10.1016/j.physd.2019.132306>
- [101] Xiao, C., Sun, J.: *Recurrent Neural Networks (RNN)*, pp. 111–135. Springer, Cham (2021). [https://doi.org/10.1007/978-3-030-82184-5\\_7](https://doi.org/10.1007/978-3-030-82184-5_7). [https://doi.org/10.1007/978-3-030-82184-5\\_7](https://doi.org/10.1007/978-3-030-82184-5_7)
- [102] Islam, S., Elmekki, H., Elsebai, A., Bentahar, J., Drawel, N., Rjoub, G., Pedrycz, W.: A comprehensive survey on applications of transformers for deep learning tasks. *Expert Systems with Applications* **241**, 122666 (2024) <https://doi.org/10.1016/j.eswa.2023.122666>
- [103] Khan, S., Naseer, M., Hayat, M., Zamir, S.W., Khan, F.S., Shah, M.: Transformers in vision: A survey. *ACM Comput. Surv.* **54**(10s) (2022) <https://doi.org/10.1145/3505244>
- [104] Mildenhall, B., Srinivasan, P.P., Tancik, M., Barron, J.T., Ramamoorthi, R., Ng, R.: NeRF: Representing Scenes as Neural Radiance Fields for View Synthesis (2020). <https://arxiv.org/abs/2003.08934>
- [105] Yu, A., Ye, V., Tancik, M., Kanazawa, A.: pixelNeRF: Neural Radiance Fields from One or Few Images (2021). <https://arxiv.org/abs/2012.02190>
- [106] Niemeyer, M., Barron, J.T., Mildenhall, B., Sajjadi, M.S.M., Geiger, A., Radwan, N.: RegNeRF: Regularizing Neural

- Radiance Fields for View Synthesis from Sparse Inputs (2021). <https://arxiv.org/abs/2112.00724>
- [107] Zaheer, M., Guruganesh, G., Dubey, A., Ainslie, J., Alberti, C., Ontanon, S., Pham, P., Ravula, A., Wang, Q., Yang, L., Ahmed, A.: Big Bird: Transformers for Longer Sequences (2021). <https://arxiv.org/abs/2007.14062>
- [108] Wolf, T., Debut, L., Sanh, V., Chaumond, J., Delangue, C., Moi, A., Cistac, P., Rault, T., Louf, R., Funtowicz, M., et al.: HuggingFace’s Transformers: State-of-the-art Natural Language Processing (2020). <https://arxiv.org/abs/1910.03771>
- [109] HuggingFace: BigBird model (2024). [https://github.com/huggingface/transformers/tree/v4.42.0/src/transformers/models/big\\_bird](https://github.com/huggingface/transformers/tree/v4.42.0/src/transformers/models/big_bird)
- [110] Hendrycks, D., Gimpel, K.: Gaussian Error Linear Units (GELUs) (2023). <https://arxiv.org/abs/1606.08415>
- [111] Rubner, Y., Tomasi, C., Guibas, L.J.: A metric for distributions with applications to image databases. In: Sixth International Conference on Computer Vision (IEEE Cat. No.98CH36271), pp. 59–66 (1998). <https://doi.org/10.1109/ICCV.1998.710701>
- [112] Wu, T., Pan, L., Zhang, J., Wang, T., Liu, Z., Lin, D.: Density-aware Chamfer Distance as a Comprehensive Metric for Point Cloud Completion (2021). <https://arxiv.org/abs/2111.12702>
- [113] Lee, C.-Y., Xie, S., Gallagher, P., Zhang, Z., Tu, Z.: Deeply-Supervised Nets (2014). <https://arxiv.org/abs/1409.5185>
- [114] Li, R., Wang, X., Huang, G., Yang, W., Zhang, K., Gu, X., Tran, S.N., Garg, S., Alty, J., Bai, Q.: A Comprehensive Review on Deep Supervision: Theories and Applications (2022). <https://arxiv.org/abs/2207.02376>
- [115] Paszke, A., Gross, S., Massa, F., Lerer, A., Bradbury, J., Chanan, G., Killeen, T., Lin, Z., Gimelshein, N., Antiga, L., et al.: PyTorch: An imperative style, high-performance deep learning library. In: Advances in Neural Information Processing Systems 32, pp. 8024–8035. Curran Associates, Inc., Red Hook, NY, USA (2019). <http://papers.neurips.cc/paper/9015-pytorch-an-imperative-style-high-performance-deep-learning-library.pdf>
- [116] Falcon, W., The PyTorch Lightning team: PyTorch Lightning (2019). <https://doi.org/10.5281/zenodo.3828935> . <https://github.com/Lightning-AI/lightning>
- [117] Kingma, D.P., Ba, J.: Adam: A Method for Stochastic Optimization (2017). <https://arxiv.org/abs/1412.6980>
- [118] Loshchilov, I., Hutter, F.: Decoupled Weight Decay Regularization (2019). <https://arxiv.org/abs/1711.05101>
- [119] Akiba, T., Sano, S., Yanase, T., Ohta, T., Koyama, M.: Optuna: A next-generation hyperparameter optimization framework. In: Proceedings of the 25th ACM SIGKDD International Conference on Knowledge Discovery and Data Mining (2019)
- [120] Dempster, A.P., Laird, N.M., Rubin, D.B.: Maximum likelihood from incomplete data via the em algorithm. Journal of the Royal Statistical Society: Series B (Methodological) **39**(1), 1–22 (2018) <https://doi.org/10.1111/j.2517-6161.1977.tb01600.x> [https://academic.oup.com/jrsssb/article-pdf/39/1/1/49117094/jrsssb\\_39.1.1.pdf](https://academic.oup.com/jrsssb/article-pdf/39/1/1/49117094/jrsssb_39.1.1.pdf)
- [121] Alvarez-Ruso, L., Athar, M.S., Barbaro, M.B., Cherdack, D., Christy, M.E., Coloma, P., Donnelly, T.W., Dytman, S., Gouvêa, A., Hill, R.J., et al.: Nustec1 1neutrino scattering theory experiment collaboration <http://nustec.fnal.gov>. white paper: Status and challenges of neutrino–nucleus scattering. Progress in Particle and Nuclear Physics **100**, 1–68 (2018) <https://doi.org/10.1016/j.ppnp.2018.01.006>
- [122] Hen, O., Miller, G.A., Piasetzky, E.,

- Weinstein, L.B.: Nucleon-nucleon correlations, short-lived excitations, and the quarks within. *Rev. Mod. Phys.* **89**, 045002 (2017) <https://doi.org/10.1103/RevModPhys.89.045002>
- [123] Gran, R., Nieves, J., Sanchez, F., Vicente Vacas, M.J.: Neutrino-nucleus quasi-elastic and 2p2h interactions up to 10 GeV. *Phys. Rev. D* **88**(11), 113007 (2013) <https://doi.org/10.1103/PhysRevD.88.113007> [arXiv:arXiv:1307.8105](https://arxiv.org/abs/1307.8105) [hep-ph]
- [124] Nieves, J., Sanchez, F., Ruiz Simo, I., Vicente Vacas, M.J.: Neutrino Energy Reconstruction and the Shape of the CCQE-like Total Cross Section. *Phys. Rev. D* **85**, 113008 (2012) <https://doi.org/10.1103/PhysRevD.85.113008> [arXiv:arXiv:1204.5404](https://arxiv.org/abs/1204.5404) [hep-ph]
- [125] Sobczyk, J.E., Nieves, J., Sánchez, F.: Exclusive final state hadron observables from neutrino-nucleus multi-nucleon knockout. *Phys. Rev. C* **102**(2), 024601 (2020) <https://doi.org/10.1103/PhysRevC.102.024601> [arXiv:arXiv:2002.08302](https://arxiv.org/abs/2002.08302) [nucl-th]
- [126] Acero, M.A., *et al.*: Adjusting neutrino interaction models and evaluating uncertainties using nova near detector data. *The European Physical Journal C* **80**(12), 1119 (2020) <https://doi.org/10.1140/epjc/s10052-020-08577-5>
- [127] Abratenko, P., *et al.*: New CC0 $\pi$  GENIE model tune for MicroBooNE. *Phys. Rev. D* **105**, 072001 (2022) <https://doi.org/10.1103/PhysRevD.105.072001>
- [128] Abe, K., *et al.*: Measurement of neutrino and antineutrino oscillations by the T2K experiment including a new additional sample of  $\nu_e$  interactions at the far detector. *Phys. Rev. D* **96**, 092006 (2017) <https://doi.org/10.1103/PhysRevD.96.092006>
- [129] Abe, K., *et al.*: Measurements of neutrino oscillation parameters from the T2K experiment using  $3.6 \times 10^{21}$  protons on target. *The European Physical Journal C* **83**(9), 782 (2023) <https://doi.org/10.1140/epjc/s10052-023-11819-x>
- [130] Proto-Collaboration, H.-K., ;, Abe, K., Abe, K., Aihara, H., Aimi, A., Akutsu, R., Andreopoulos, C., Anghel, I., Anthony, L.H.V., Antonova, M., Ashida, Y., *et al.*: Hyper-Kamiokande Design Report (2018). <https://arxiv.org/abs/1805.04163>
- [131] Abud Abed, A., *et al.*: Low exposure long-baseline neutrino oscillation sensitivity of the DUNE experiment. *Phys. Rev. D* **105**(7), 072006 (2022) <https://doi.org/10.1103/PhysRevD.105.072006> [arXiv:2109.01304](https://arxiv.org/abs/2109.01304) [hep-ex]
- [132] Chen, T., Guestrin, C.: Xgboost: A scalable tree boosting system. In: *Proceedings of the 22nd ACM SIGKDD International Conference on Knowledge Discovery and Data Mining, KDD '16*, pp. 785–794. Association for Computing Machinery, New York, NY, USA (2016). <https://doi.org/10.1145/2939672.2939785> . <https://doi.org/10.1145/2939672.2939785>

## Acknowledgements

This work was supported by the Swiss National Science Foundation under grant PCEFP2\_203261. This research was also partially supported by the Swiss National Science Foundation (grant 20QT21\_187716 Qu3D “Quantum 3D Imaging at high speed and high resolution”). Neural network training in this work used resources of the National Energy Research Scientific Computing Center (NERSC), a U.S. Department of Energy User Facility, under the AI4Sci@NERSC award DDR-ERCAP0034642. Additional training support was provided through the Swiss AI Initiative via a grant from the Swiss National Supercomputing Centre (CSCS), project ID a149, on the Alps system. We would like to thank Prof. André Rubbia from ETH Zurich for useful inputs and discussions and for providing access to laboratory equipment and facilities; Prof. Vincenzo Berardi at Politecnico di Bari, Dr. Umut Kose and Johannes Wüthrich from ETH Zurich for useful discussions; Arne Erdmann from Raytrix GmbH

for helping to understand the functioning of the plenoptic camera prototype assembled at Raytrix and the use of the RxLive software; Prof. Wallny at ETH Zurich for providing access to his group's thermal chamber.

## **Author contributions**

D.S. conceived the PLATON detector, is the PI of the project funded by the Swiss National Science Foundation, and supervised every aspect of the project. T.D. was the main analyser and developer. The plenoptic system of the prototype was designed and built by Raytrix GmbH. E.C., C.B., and K.K. provided the SPAD array photosensor, assisted with its use, offered guidance, and supervised the project to ensure understanding of the results. T.D., T.W., and M.F. set up the tests in the laboratory. T.D. ran the experiments, developed the software and analysed the data. T.D., S.A.-M., and D.S. conceived the standard image post-processing method, and T.D. developed and tested it. T.D. developed and tested the software for the simulation of the detector. T.D. studied the detector configuration of the simulated physics experiments. Also, C.A. worked on the detector simulation. S.A.-M. conceived, developed, trained, and validated the neural-network-based image post-processing. N.B., S.A.-M., and T.D. performed the pattern recognition and data analysis of the simulated neutrino experiment. All the authors contributed to the writing of the paper.

## **Disclaimer notice**

This document was prepared by Swiss Federal Institute of Technology-Zurich (ETH Zurich), in part as a result of the use of facilities of the U.S. Department of Energy (DOE), which are managed by The Regents of the University of California, acting under Contract No. DE-AC02-05CH11231. Neither The Regents of the University of California, DOE, the U.S. Government, nor any person acting on their behalf: (a) make any warranty or representation, express or implied, with respect to the information contained in this document; or (b) assume any liabilities with respect to the use of, or damages resulting from the use of any information contained in the document.